Coronal Densities, Temperatures and Abundances During the 2019 Total Solar Eclipse: The Role of Multi-Wavelength Observations in Coronal Plasma Characterization

Giulio Del Zanna,[1] Jenna Samra,[2] Austin Monaghan,[3] Chad Madsen,[2] Paul Bryans,[3] Edward DeLuca,[2] Helen Mason,[1] Ben Berkey,[3] Alfred de Wijn,[3] and Yeimy J. Rivera[2]

[1]*DAMTP, CMS, University of Cambridge, Wilberforce Road, Cambridge CB3 0WA, UK*
[2]*Center for Astrophysics | Harvard & Smithsonian, 60 Garden Street, Cambridge, MA, 02138, USA*
[3]*HAO, National Center for Atmospheric Research, P.O. Box 3000, Boulder CO 80307-3000, USA*

ABSTRACT

The Airborne Infrared Spectrometer (AIR-Spec) offers an unprecedented opportunity to explore the Near Infra-Red (NIR) wavelength range. It has been flown at two total solar eclipses, in 2017 and 2019. The wavelength range of the much improved instrument on the second flight (July 2, 2019) was shifted to cover two density sensitive lines from S XI. In this paper we study detailed diagnostics for temperature, electron density and elemental abundances by comparing results from AIR-Spec slit positions above the east and the west limb with those from Hinode/EIS, the PolarCam detector and SDO/AIA. We find very good agreement in the electron densities obtained from the EIS EUV line ratios, those from the NIR S XI ratio and those obtained from the polarized brightness PolarCam measurements. Electron densities ranged from Log Ne [cm^{-3}] = 8.4 near the limb, falling to 7.2 at $R_0 = 1.3$. EIS spectra indicate that the temperature distribution above the west limb is near-isothermal at around 1.3 MK, while that on the east has an additional higher-T component. The AIR-Spec radiances in Si X and S XI as well as the AIA data in the 171, 193, and 211 Å bands are consistent with the EIS results. EIS and AIR-Spec data indicate that the sulphur abundance (relative to silicon) is photospheric in both regions, confirming our previous results of the 2017 eclipse. The AIA data also indicate that the absolute iron abundance is photospheric. Our analysis confirms the importance of the diagnostic potential of the NIR wavelength range, and that this important wavelength range can be used reliably and independently to determine coronal plasma parameters.

Keywords: Solar coronal lines (2038); Solar instruments (1499); Total eclipses (1704); Spectrometers (1554)

1. INTRODUCTION

The visible forbidden lines provided the first detailed information about the plasma conditions in the solar corona, with several spectroscopic observations carried out in the 1950's to 1970's (see the review in Del Zanna & DeLuca 2018). Since then, most observations have been carried out at shorter wavelengths in the XUV. However, there is now renewed interest in the forbidden lines in the visible and especially in the near-infrared (NIR). This is partly because these lines are signifi-

Corresponding author: Giulio Del Zanna

cantly enhanced due to photo-excitation (PE) from the solar disk radiation, hence are easier to measure out to greater distances from the solar limb, compared to the XUV lines, as shown e.g. by Habbal et al. (2011) using observations of visible lines.

There have been many studies from the ground based on the visible lines during total eclipses, as for example Ding & Habbal (2017); Koutchmy et al. (2019). For a recent review of such observations see Habbal et al. (2021).

In this paper, we focus on the NIR lines, as they offer the possibility for routine coronal magnetic field measurements via the Zeeman and Hanle effects (see, e.g. Judge 1998; Judge et al. 2001), partly thanks to recent improvements in NIR detectors. Also, measurements

of non-thermal widths are easier to obtain in the NIR than the EUV (for a recent attempt to measure non-thermal line widths in the EUV see Del Zanna et al. 2019). The NIR lines offer in principle the same spectral diagnostic applications as the XUV lines, in terms of measurements of electron densities, temperatures, and elemental abundances from line ratios (see Del Zanna & DeLuca 2018). Such measurements are fundamental constraints to physical models of the middle corona, the almost unexplored region between 1.5 and 3 solar radii, as reviewed by West et al. (2022).

Densities and temperatures are obvious key parameters. It has been recognised in the literature that it is also important to measure elemental abundances. It is now well established that coronal abundances, depending on the feature observed, are different to the photospheric ones. Variations are strongly correlated with the FIP (First Ionization Potential) of an element, with generally low FIP elements being enhanced, relative to the high-FIP ones (the so-called FIP effect). The variations are likely related to the plasma heating processes in the chromosphere (where neutrals are ionized). Also, in principle they are not significantly modified once established in the corona, so could be used as a tracer of the origin of the solar wind streams, whenever elemental abundances are measured in-situ. For details, see the Solar Living Reviews by Laming (2015) and Del Zanna & Mason (2018).

For the above (and other) reasons, several missions have recently included diagnostics of NIR lines. Various space-based missions such as ESA's Proba-3 and the first Indian large solar mission Aditya will observe several forbidden lines. On the ground, UComp, an improved version of the successful Coronal Multi-Channel Polarimeter (CoMP) is now operational (Landi et al. 2016; Tomczyk & Landi 2019; Tomczyk et al. 2021). A major new facility is the Daniel K. Inouye Solar Telescope (DKIST, Tritschler et al. 2016; Rimmele et al. 2020). The main coronal instrument, the Cryogenic Near Infrared Spectropolarimeter (Cryo-NIRSP, https://atst.nso.edu/inst/cryonirsp) will make regular observations, but only close to the solar limb and with a small field of view (FOV). In addition, we note that any ground-based telescope is strongly limited by atmospheric absorption, except in a few spectral regions.

Cryo-NIRSP is planning to observe a few lines that are known to be observable, but the NIR is in principle rich in other diagnostics. As the NIR is an almost unexplored spectral region in solar physics, the Airborne Infrared Spectrometer (AIR-Spec, Samra et al. 2022) was funded by the NSF and developed by Smithsonian Astrophysical Observatory (SAO) to explore the NIR.

The instrument has observed the quiescent solar corona during two eclipses, in 2017 and 2019, flying onboard the NSF/NCAR Gulfstream V (GV) at an altitude of 12 km, where atmospheric absorption is much reduced. The long slit of the instrument allows measurements of the outer corona, at far greater heights than Cryo-NIRSP.

The 2.853 µm Fe IX line was detected for the first time during the first flight (Samra et al. 2018; Samra et al. 2019). Multi-wavelength observations during the 2017 eclipse were presented in Madsen et al. (2019), and used to measure electron densities, ionization temperatures (i.e. temperatures obtained from lines of different ions, assuming ionization equilibrium), and elemental abundances. The results were close to those obtained from an analysis of earlier SoHO SUMER and UVCS observations of quiescent streamers during solar minimum (Del Zanna et al. 2018). The electron densities were obtained from EUV line ratios observed by the Hinode Extreme Ultraviolet Imaging Spectrometer (EIS, Culhane et al. 2007). Emission measures obtained from both AIR-Spec and EIS indicated a near-isothermal temperature distribution, and, perhaps surprisingly, nearly photospheric abundances (Asplund et al. 2009) in terms of relative abundance between Sulphur and Silicon.

The second flight observed the July 2, 2019 total solar eclipse with a much improved and modified instrument. The wavelength coverage was shifted so as to observe the 1.4 µm S XI line, to obtain electron densities directly from the ratio with the 1.9 µm S XI line. The observations and preliminary results from this eclipse are described in Samra et al. (2022). The observations were successful and the 1.4 µm S XI line was recorded for the first time, although careful atmospheric modeling was required to measure its intensity.

As we did in 2017, we coordinated multi-wavelength observations for the 2019 eclipse, in particular with the Hinode EIS instrument and the ground-based PolarCam, a novel micro-polarizer camera. The effectiveness of this camera for solar observing was demonstrated during the 2017 total solar eclipse, where polarized brightness (pB) measurements showed good agreement with the pB observations of the dedicated solar observatory COSMO K-Coronagraph (K-Cor) in Mauna Loa, Hawaii (Judge et al. 2019). For the 2019 eclipse described here, the High Altitude Observatory (HAO) in Boulder organised an expedition to the Cerro Tololo Inter-American Observatory (CTIO) in Chile, taking polarization measurements in white light with PolarCam.

We note that other studies of the 2019 eclipse, based on observations in the visible, have been published. Boe et al. (2022) presented narrowband images, and Hanaoka
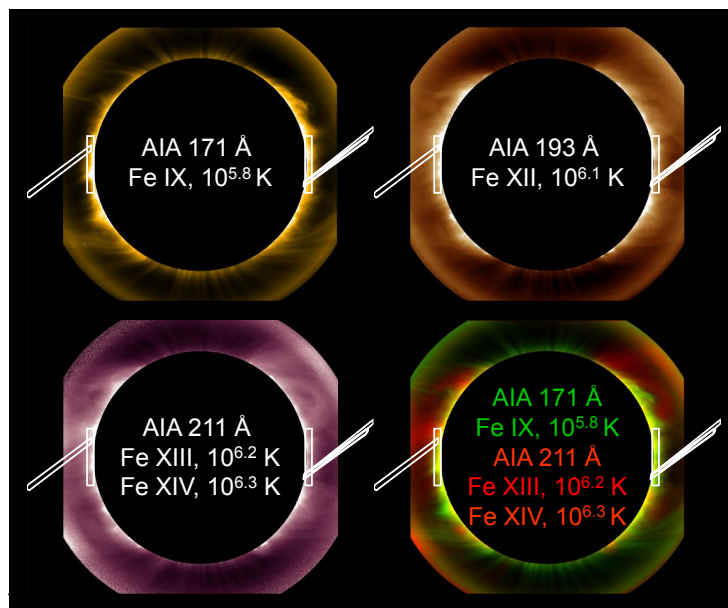
Figure 1. False-color images of the solar corona during the 2019 total eclipse in three SDO AIA channels. The bottom right image is a composite obtained from AIA 171 Å (green) and 211 Å (red). The AIR-Spec slits and EIS fields of view are shown in white.
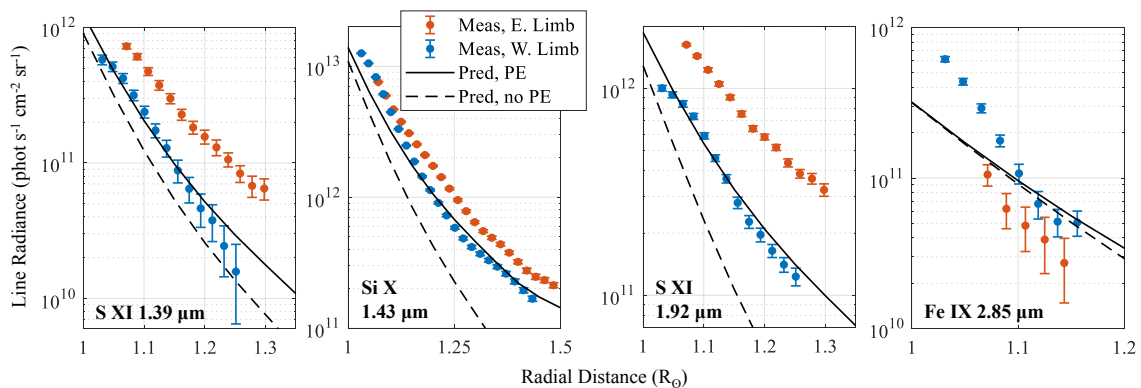
Figure 2. Predicted and measured radiance of the main four AIR-Spec lines above the east and west limbs. The hotter S XI lines are stronger above the east limb while the cooler Fe IX line is stronger above the west limb. Predictions with (full line) and without (dashed line) photoexcitation were made using the quiescent streamers density model of Del Zanna et al. (2018) and an isothermal temperature of 1.3 MK. This model fits the west region best, but does not represent well the east region.

et al. (2021) used pB continuum images. In this paper, we present an analysis of the AIR-Spec data, to obtain measurements of electron densities, ionization temperatures, and elemental abundances. We validate and compare these results to those obtained from Hinode EIS, PolarCam, and SDO AIA observations.

2. ECLIPSE OBSERVATIONS

2.1. *AIR-Spec*

AIR-Spec observed for about 7 minutes during totality on July 2, 2019 (19:18:16 – 19:26:48 UT) in 9 slit positions. Details of the observation and data processing are described in Samra et al. (2022). The main lines

that were observed are listed in Table 1, with their typical formation temperatures (the ranges of temperatures where these lines can be formed are shown in the Appendix in Figure 12). We discuss here the observations on the east and west limb, which are co-spatial with the Hinode EIS observations.

Figure 1 shows a false-color SDO AIA image obtained from the 171 Å (green) and 211 Å (red) channels, and the locations of the AIR-Spec east and west slits, as well as the pointings of the EIS slit close to the limb. It is well established that in the outer corona the 171 Å broadband is dominated by Fe IX, formed around 1 MK, while the 211 Å has a significant contribution from Fe XIV,
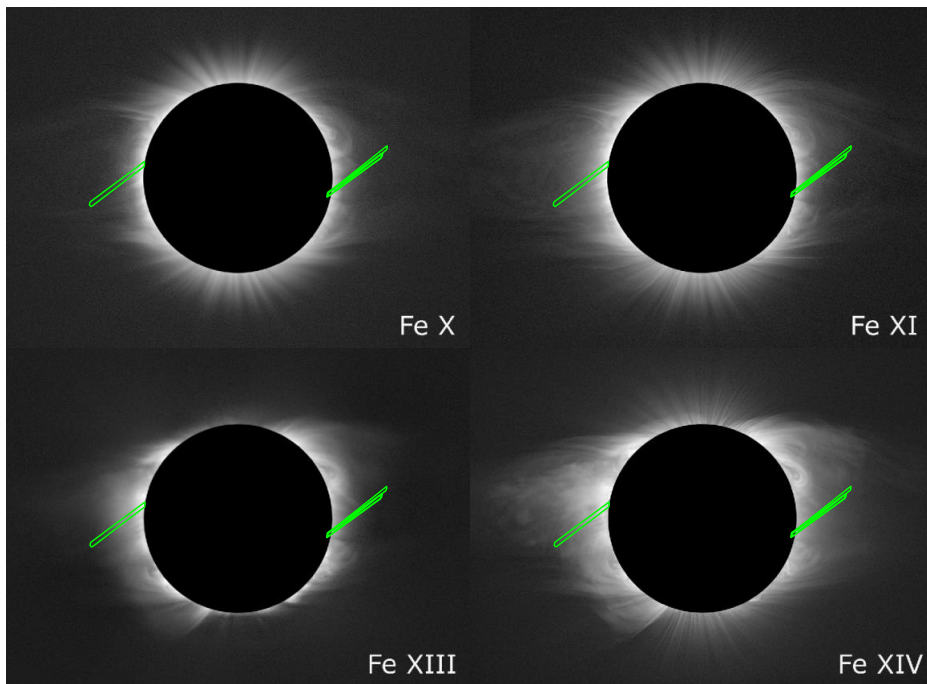
Figure 3. Narrowband images of the solar corona during the 2019 total eclipse in Fe X 637.4 nm, Fe XI 789.2 nm, Fe XIII 1074.7 nm, and Fe XIV 530.3 nm (private communication S. Habbal to J. Samra, image credit S. Habbal and M. Druckmüller). The AIR-Spec slits are overlaid in green.

Table 1. AIR-Spec target lines.

Ion	λ (nm)	T (MK)	Transition (Upper $\to$ Lower)
S XI	1393	1.9	$2s^2 2p^2\ ^3P_2 \to 2s^2 2p^2\ ^3P_1$
Si X	1431	1.3	$2s^2 2p\ ^2P^o_{3/2} \to 2s^2 2p\ ^2P^o_{1/2}$
S XI	1921	1.9	$2s^2 2p^2\ ^3P_1 \to 2s^2 2p^2\ ^3P_0$
Fe IX	2853	0.8	$3s^2 3p^5 3d\ ^3F^o_3 \to 3s^2 3p^5 3d\ ^3F^o_4$

formed around 2 MK, together with contributions from several other coronal lines formed at lower temperatures such as those from Fe XIII. It is therefore already clear from Figure 1 that the corona in the east limb is hotter than that on the west. We will return to this issue below.

The actual pointing of the AIR-Spec slit varied in time during the eclipse. The precise pointing of each exposure was obtained using the context images from the white light slit-jaw camera. As the solar corona was quiescent, exposures were averaged and data spatially binned to increase the signal to noise.

We obtained measurements of the radiances of S XI 1.393 and 1.921 µm, as well as the strong Si X 1.431 µm and the weaker Fe IX 2.853 µm above the east and west limb, as shown in Figure 2. It is clear that the corona in the west and east is similar in Si X, which is formed around 1.3 MK, while it is significantly different as seen

in S XI which is normally formed at higher temperatures. In principle, the differences in the two regions could also be due to different Si/S relative abundances, although we will show below that the difference is actually due to higher temperatures being present in the east.

Figure 2 also shows the values predicted from the quiescent streamers density model of Del Zanna et al. (2018), photospheric abundances and an isothermal temperature of 1.3 MK, on the basis of the measurements discussed below. It is clear that such a model represents quite well the radiances in the west region. We do not attempt to model the east region as it is multi-thermal.

In Figure 3, we show the AIR-Spec slits overlaid on the narrowband images described in Boe et al. (2022). The narrowband images are credited to S. Habbal and M. Druckmüller and were provided to J. Samra in a private communication from S. Habbal. It is clear from the Fe XIII and Fe XIV overlays that AIR-Spec sampled hotter material on the east limb than on the west, which agrees with the electron temperature inferred in Boe et al. (2022). Section 3.3 provides quantitative support for this conclusion.

2.2. EIS

Hinode EIS carried out two main 'rasters', where the $2''$ slit scanned a $60''$ off-limb region with 120 s expo-

sure times, resulting in a total duration of about one hour. The first raster started at 18:36:42 UT above the east limb, and ended at 19:37:37, just after the end of totality. The second raster started shortly after the end of totality, at 20:15:41 UT, and scanned a region above the west limb. The full EIS spectral range, i.e. all of the short (SW) and long (LW) wavelength channels were telemetered. The maximum number of detector pixels along the slit, 512, were telemetered.

The EIS data were processed with custom-written software (see, e.g. Del Zanna et al. 2011) which largely follows the standard SolarSoft EIS_PREP program. The hot and warm pixels (i.e. pixels with anomalous counts), and those affected by particle events are flagged as 'missing'. We used the SolarSoft database for the hot and warm pixels. One difference with the standard software is that the missing pixels are then replaced with values interpolated along different directions, and the results are visually inspected. Despite this procedure, the spectra are very noisy. First, this is because of the low signal. Second, this is because the long exposures resulted in a large number of cosmic ray hits. Third, this is because the EIS detector has degraded so much in the past few years that a large area is affected by warm pixels, only some of which are included in the database. Other differences with the standard software are that the spectra are rotated, to remove the geometrical slant, and the fitting of the lines is carried out on the spectra in data numbers (DN), fitting the bias with a polynomial. To further proceed with the EIS analysis, we encountered two major problems, concerning the radiometric calibration and the pointing, as described below.

2.2.1. *EIS radiometric calibration*

An accurate radiometric calibration, at least in relative terms, is necessary to measure all the key plasma parameters. For example, the best measurements for the electron density for the present observations are obtained from the ratio of the Fe XII 186.8 and 192.4 Å lines, as other diagnostic lines e.g. from Fe XIII were very weak. The relative calibration at 186.8 and 192.4 Å is not well known and has been changing over time. Del Zanna (2013a) presented a significant revision of the ground calibration which only applied to data up to 2012. Indications of time-dependent changes were also found, a problem later confirmed by Warren et al. (2014). Warren et al. analysed some observations of the quiet Sun off-limb, and imposing isothermality obtained a relative calibration for data until 2014. We have extended this approach and performed a DEM analysis of a quiet Sun off-limb observations close in time, on 2019-06-28 at 09:38 UT, with the 2″ slit and 60 s exposures.

The relative calibration was obtained by matching the observed radiances to the predicted ones, using CHIANTI version 10 (Del Zanna et al. 2021).

The established relative calibration for the short-wavelength (SW) channel was then used to cross-calibrate the EIS spectra against simultaneous SDO AIA 193 Å observations, taking into account the different spatio-temporal resolutions, following the methods described in Del Zanna et al. (2011); Del Zanna (2013b). In turn, the AIA calibration relies on the SDO EVE calibration, although we note that this could be done only until 2014. The AIA degradation in 2019 was extrapolated from the cross-calibration EVE sounding rocket flown in 2018, although that is currently being revised taking into account the latest EVE sounding rocket flown in Sept 2021.

Details are provided in the Appendix, in Section E. The absolute and relative calibrations have typical uncertainties of 20%. The above methods have been extended to provide an EIS calibration for the entire mission, which is the subject of another paper.

2.2.2. *EIS Pointing*

The precise pointing of the EIS instrument is generally not known. The EIS pointing is relatively stable, except a 2–3″ jittering on fast time scales, probably caused by small flexures inside the long (3 mt) structure holding the optics. Usually, the pointing is established by a cross-correlation with EUV images. As the off-limb observations considered here do not present any clear features, the only way we could estimate the pointing was to compare EIS with the AIA 193 Å data, as described in the Appendix, in Section F.

2.3. *PolarCam*

The PolarCam experiment was sited at CTIO, under the path of totality in northern Chile, at an altitude of 2200 m. While not high enough to significantly mitigate telluric absorption, the location has favourable cloud cover, sitting above the stratus layer, as well as offering the infrastructure of an existing observatory. The experiment successfully observed totality from 20:38:45 to 20:40:53 UT on 2019 July 2.

The 4D Technologies PolarCam consists of a micropolarising array placed over a CCD detector. Each superpixel has four subpixels with alternating orientations of linear polarisation: 0, 45, 90, and 135 degrees. Images of the total linear polarisation can then be constructed from these four polarisation states. Its small size and lack of moving parts make such a camera an ideal candidate for a future CubeSat mission. For the July 2019 eclipse, we mounted the camera on a Stellarvue 70 mm f/6 refracting telescope behind a bandpass filter centred

at 734 nm with 46 nm FWHM. Acquired images have 1920×1200 pixels, with 2.91 arcsec sampling and 70 ms exposures.

3. PLASMA CHARACTERIZATION

3.1. *Electron Density*

3.1.1. *Density estimates from polarized brightness measurements*

The PolarCam data were calibrated by subtracting a dark image that was taken with the shutter closed immediately following the eclipse. They were flat fielded by taking the same exposures but using an opal glass attenuator, performed 24 hours before the eclipse to mimic conditions as closely as possible. We also investigated the contribution of sky polarization to the measurements and found it to be negligible (in contrast to the measurements of Hanaoka et al. 2021). This is to be expected, given that the sky is several orders of magnitude darker during eclipse, leading to a negligible contribution to the polarization from the sky.

The calibrated results of the subpixels with varying polarization state were combined to produce an estimate of pB for the PolarCam field of view. As in the 2017 eclipse (Judge et al. 2019), these pB results were compared wuth those of K-Cor and found to be in good agreement. This comparison also gives a verification of the PolarCam plate scale and rotation angle, which were determined independently. The plate scale was determined by measuring the limb of the Moon and comparing relative sizes of Sun and Moon for the ephemerides of CTIO.[1] Solar north was determined by measuring the locations of Bailey's Beads at second and third contact and using a Watts Chart (Watts 1963) to rotate our image. These charts of the lunar limb show the location of irregularities from a smooth sphere, allowing us to correlate the position of the bright Bailey's Beads with lunar (and hence solar) north. This method of determining the rotation angle of the PolarCam with respect to solar north was found to be consistent with a cross-correlation of the data with K-Cor.

A 60 s average of the pB measurements, from 20:39:00 to 20:39:59 UT, was used to infer the electron density. We followed the standard assumption of spherical symmetry for the density distribution of the diffuse outer quiescent corona, and obtained the radial variation of the electron density by inversion of white-light pB measurements following van de Hulst (1950). The results are shown in Figure 4.

---

[1] https://ssd.jpl.nasa.gov/horizons/
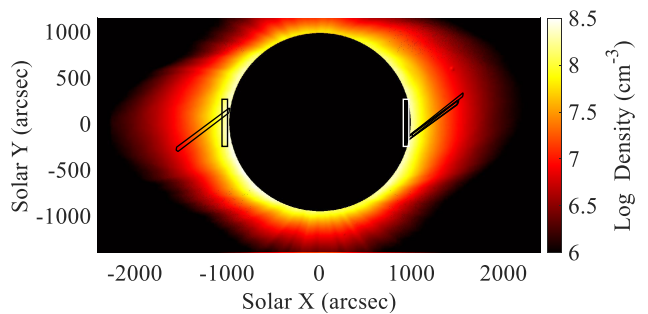
Figure 4. Electron densities obtained from the HAO Polar-Cam during the 2019 total eclipse. The AIR-Spec slits and EIS FOV are overlaid.

3.1.2. *Density estimates from IR and EUV line ratios*

Line-of-sight (LOS) averaged electron densities can be obtained directly from the AIR-Spec S XI ratio, at least out to radial distances where there is enough signal in the weaker line. However, these density measurements depend significantly on the distribution of densities along the LOS. In fact, the intensities of the forbidden lines in the NIR are significantly pumped by PE from the solar disk radiation, and not just excited by electron collisional excitation (CE) and cascades. Therefore, the observed intensities are only partially directly proportional to the square of the local electron density, as the allowed transitions are. Closer to the Sun, CE dominates over PE, but further out, depending on the local density, PE becomes dominant. In other words, it is impossible to obtain accurate electron densities from the forbidden lines unless a model for the local density distribution is assumed. More details on this issue are presented in the Appendix, in Section C.

The obvious choice for the diffuse outer corona is spherical symmetry, also to get consistency with the analysis of the PolarCam observations. We used this assumption to model the above-mentioned radiances of the SoHO SUMER and UVCS lines (Del Zanna et al. 2018), and to obtain densities from the Fe XIII 1 μm NIR forbidden lines observed by CoMP to obtain estimates of the coronal magnetic field (Yang et al. 2020).

Clearly, if the density distribution is not uniform, the densities obtained from the forbidden lines would be different to those obtained from the allowed transitions. In general, the forbidden lines have a significant contribution from very large (low-density) distances along the LOS, while the intensity of the allowed transitions mostly originates from the highest density regions. A comparison of the densities obtained from these two diagnostics therefore provides useful information on the density distribution. Such a comparison was carried out by Dudík et al. (2021), using the Fe XIII NIR forbidden

lines observed by CoMP and the Hinode EIS allowed transitions from Fe XIII and Fe XII. Very good agreement in the LOS-averaged densities from the NIR and EUV lines was obtained in an active region loop structure, once the background/foreground emission of the diffuse corona was subtracted.

It is worth noting that densities from allowed transitions are not always independent of PE effects either. In fact, the populations of the states in the ground configuration, which are key to obtaining densities also from the allowed transitions, can be affected by the solar disk radiation. This does not occur in Fe XII, as most of the transitions in the ground configuration are around 2000–3000 Å, where there are not many photons from the disk, but it is not an insignificant effect in Fe XIII, as the pumping of the 1 μm NIR forbidden lines changes the population of the ground configuration, especially the ground state. This changes the intensities of all the lines, even those decaying to the ground state, such as the strong 202 Å line.

On a positive note, as shown by Del Zanna & DeLuca (2018), the PE disk radiation can easily be included within the CHIANTI programs assuming a black-body radiation at 6100 K, as it is close to direct 1.4–2.5 μm NIR measurements from e.g. SORCE.

For EIS, we have selected the regions observed by the AIR-Spec slit, obtained averaged radiances and densities using CHIANTI version 10 from three line ratios. Figure 5 (left plots) shows a summary of the densities for the east and west. The densities from the three ratios are in agreement, within the uncertainties (see the Appendix, Figure 18). The plots also show the densities from the AIR-Spec line ratio. Again, we see very good agreement, despite the fact that the observations were not strictly simultaneous. This is to be expected as little variability was present. The AIR-Spec densities were obtained including PE.

As mentioned, the actual radial densities would be slightly higher, as the line-of-sight are averaged values. Figure 5 (right plots) shows the radial densities obtained from the AIR-Spec measurements assuming spherical symmetry, as well as those from the PolarCam observations. The results are in agreement, within uncertainties, and close to the quiescent streamers radial density model by Del Zanna et al. (2018).

3.2. *Emission measure and relative elemental abundances from EIS*

We have taken averaged EIS spectra in the east and west regions also observed by Air-Spec, around 0.09 $R_\odot$ above the limb. Parts of the EIS spectra are shown in the Appendix, in Figure 14. The strongest lines are from Fe X–Fe XIII, Si X and S X. It is clear from the spectra that the east region had significant emission in the hotter Fe XIII and Fe XIV, and also Fe XV, which was not visible above the west limb.

We estimated the differential emission measure (DEM) using a modified version of the CHIANTI_DEM routine, where the DEM is modelled with a spline. We used CHIANTI v.10, and to calculate the line emissivities assumed a constant density of $1.5\ 10^8$ cm^{-3} (although the main lines have contribution functions that are independent of density). We assumed the photospheric abundances of Asplund et al. (2009). Figure 6 shows the results, while more details on the lines are given in the Appendix, in Section D. It is clear that the distribution is nearly isothermal above the west limb, with a peak around 1.3 MK, while the distribution is more multi-thermal and shifted towards higher temperatures on the east region.

The sulphur abundance is well constrained by the S X 264.2 Å line. Other weaker lines from S X and S XI are also present and consistent with S/Si and S/Fe photospheric abundances, as shown in the Appendix in Section D. S X is formed at the same temperature as Si X and Fe XII, so the relative S/Si or S/Fe abundance is well constrained. As sulphur, in remote-sensing observations, behaves like a high-FIP element as do Ne and Ar, as described in the Appendix A, this is a strong indication that the quiescent streamers had photospheric abundances, in agreement with previous observations, as reviewed in the Appendix A. AIR-Spec and AIA observations are consistent with these results, as discussed below.

3.3. *Temperatures*

The electron temperature is a key parameter seldom measured in the corona. We refer the reader to Del Zanna & Mason (2018) and to the brief review in Appendix B. What we measure in this paper is the ionization temperature, i.e. the electron temperature from emission measure or line ratio analyses, assuming that the quiet corona is in ionization equilibrium. Such an assumption is reasonable for the quiescent streamers, and has been validated with direct measurements of the electron temperature near the limb.

As we describe in the Appendix, there is evidence in the literature that the temperature distribution also in off-limb QS regions and in quiescent streamers, up to 3 $R_\odot$, is nearly isothermal, with values around 1.3–1.4 MK. We have seen in the previous section that the Hinode EIS observations do indicate a near-isothermal distribution above the west limb, at 1.08 $R_\odot$. Therefore, the use of line (or imaging) ratios to measure 'isother-
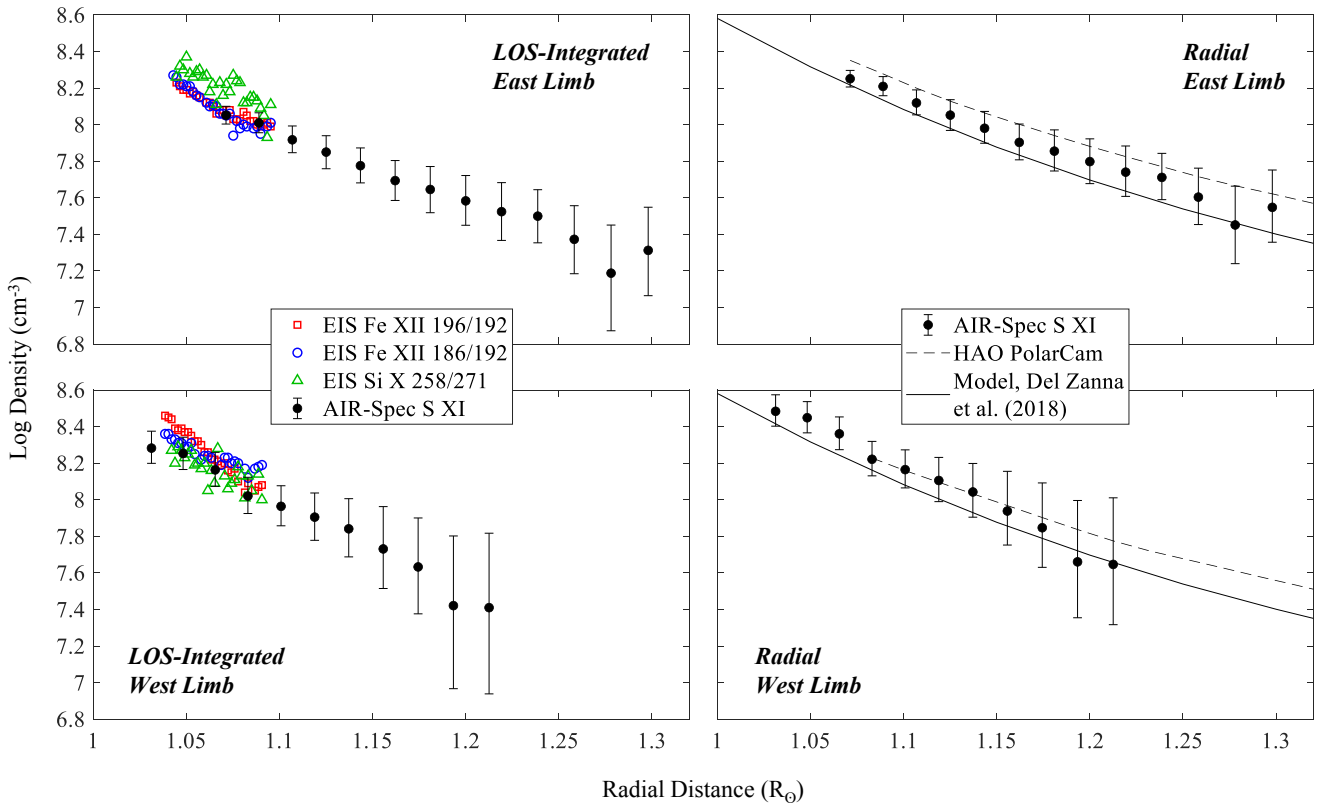
Figure 5. Electron densities on the east and west limbs during the 2019 total eclipse. The left-hand plots compare densities obtained from EIS and AIR-Spec without correcting for LOS effects. The right-hand plots compare radial density measurements obtained from AIR-Spec and PolarCam with the radial density model in Del Zanna et al. (2018).

mal temperatures' is justified. Clearly, if the plasma is strictly isothermal one would expect to find the same isothermal temperatures from the various ratios.

As pointed out in the Appendix B, there is also evidence in previous literature that, except very close to the solar limb, the temperature is almost constant with distance, at least up to 3 $R_\odot$ (still assuming ionization equilibrium, but without validation).

### 3.3.1. *Isothermal Temperatures from AIA, EIS and AIR-Spec line ratios, and S/Si relative abundance from AIR-Spec*

We have calculated the AIA responses as a function of temperature for the main coronal bands, at 171, 193 and 211 Å, using CHIANTI v10 (Del Zanna et al. 2021) atomic data and programs and the available AIA effective areas, obtained from SolarSoft with the EVENORM option (in this way the AIA areas are scaled to agree with EVE), and a constant electron density of 10^8 cm^{-3}. We used the photospheric abundances of Asplund et al. (2009), but note that the AIA coronal bands are all dominated by iron lines (see, e.g. Del Zanna et al. 2011), so the isothermal temperatures are independent of the choice of elemental abundances. The AIA 193 vs 171 Å

and 211 vs. 171 Å ratios are strongly dependent on the ionization temperature, while the 211 vs. 193 Å is not sensitive to temperatures around 1.4 MK, being flat and multi-valued.

We downloaded the AIA data with a cadence of 2 minutes, during the two hours of the EIS observations. There are only minor changes in the solar corona during the EIS rasters. However, for each EIS exposure, we took the AIA images closest in time and obtained averaged AIA DN/s in the two bands for the EIS regions co-spatial with the locations of the AIR-Spec slits.

Figure 7 (panel b) shows the isothermal temperatures obtained from the AIA filter ratios. It is clear, as we have already anticipated, that the eastern region is hotter than the western one. Figure 7 (panel a) shows a few isothermal temperatures obtained from EIS iron lines. There is generally good agreement between the EIS and AIA results, confirming that the eastern region is hotter and more multi-thermal than the western one, in agreement with the EIS DEM results. However, we point out that the two AIA filter ratios produce an effective temperature biased by the thermal distribution and the AIA responses, as discussed below.
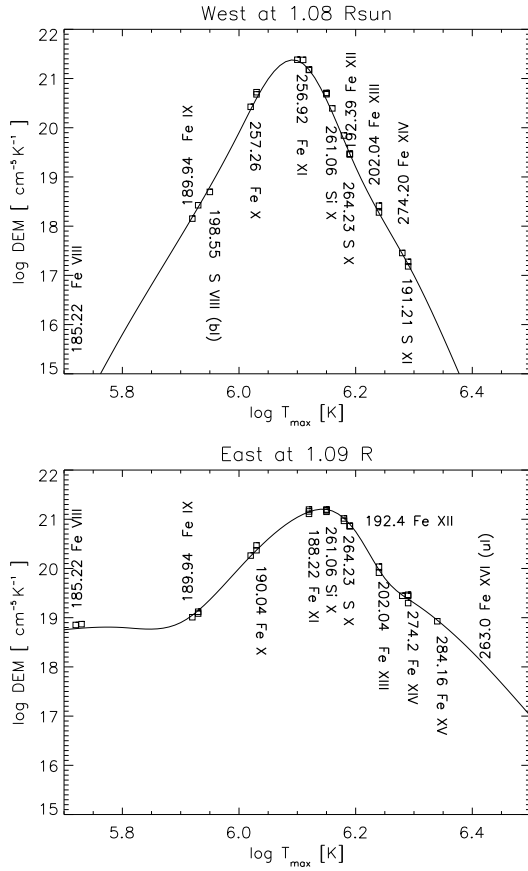
Figure 6. The DEMs for the off-limb west and east regions obtained from Hinode EIS. The points are plotted at the temperature T_{max} of maximum emissivity, and at the theoretical vs. the observed intensity ratio multiplied by the DEM value. The wavelength (Å) and ions of a few key lines are shown.

We have also calculated the AIA temperatures by averaging images during the 2 minutes of the total eclipse, for a direct comparison with the AIR-Spec data. The results are shown in Figure 7, bottom panel, and in Figure 8.

Unlike the previous 2017 observation, where a few lines were observed and enabled us to produce an emission measure loci, in the present case we only have two AIR-Spec lines to estimate the ionization temperature: Si X 1.431 µm and S XI 1.921 µm out to 1.3 $R_{\odot}$, as the Fe IX 2.853 µm is too weak at large distances. The Si X vs. S XI ratio is in principle a good temperature diagnostic for quiescent streamers, but there are two issues. The first regards the relative elemental abundances of Si and S. As the relative S/Si abundances as measured by EIS at 1.08 $R_{\odot}$ are photospheric, we expect them to be the same at larger distances, so we used the same
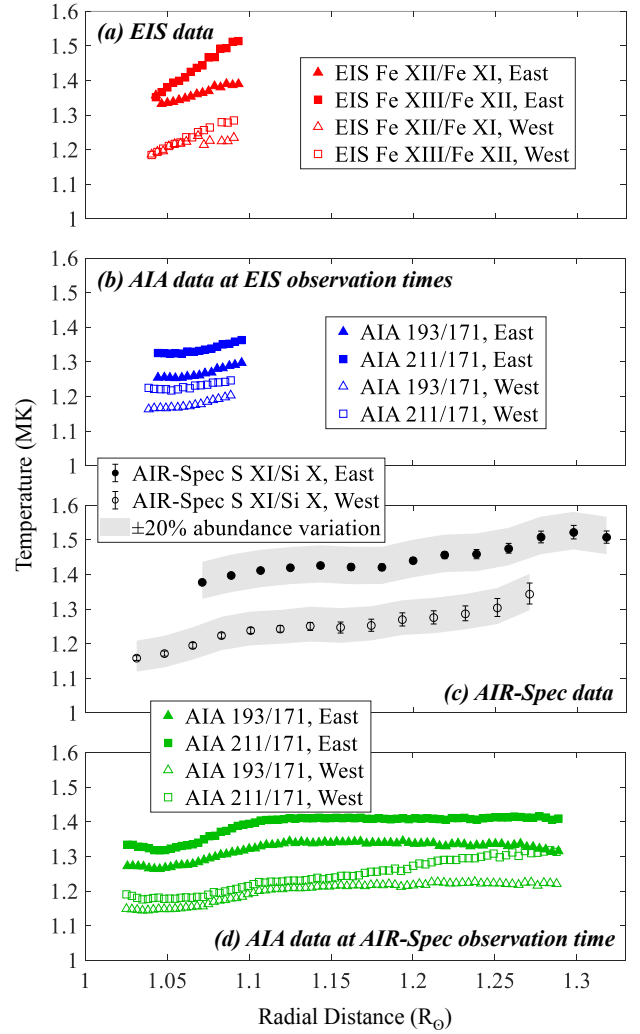

Figure 7. Isothermal temperatures in the east and west quiescent streamers regions covered by the AIR-Spec slits. The top two plots show temperatures obtained from simultaneous EIS (a) and AIA (b) observations. The bottom two plots show temperatures obtained from simultaneous AIR-Spec (c) and AIA (d) observations.

S/Si abundances to calculate the isothermal temperature from the NIR ratio.

The second issue relates to the above-mentioned complication that the LOS radiances not only depend on density and temperature, but also on the relative importance of the CE and PE processes.

We have adopted the model of spherical symmetry, photospheric abundances and the densities we obtained from the S XI ratio, to predict the Si X vs. S XI LOS radiances as a function of temperature (see details in the Appendix, Section C). By comparison with the observed ratio of the radiances, we then obtained the isothermal temperatures from the NIR ratio. The values are shown
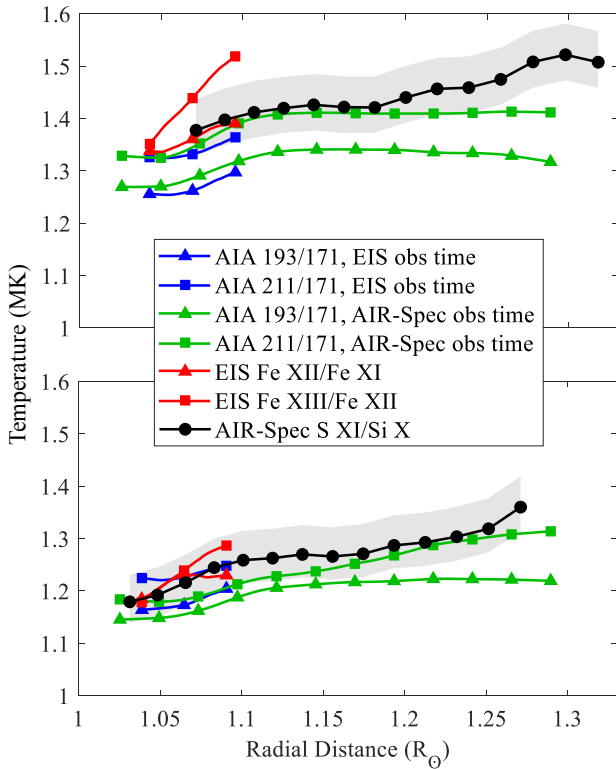
Figure 8. Overlay of temperatures from EIS, AIR-Spec and AIA observations in the east (top) and west (bottom). For clarity, the data from Figure 7 have been smoothed before plotting.

as diamonds in Figure 7, panel c and as circles in Figure 8.

The gray shaded area in Figures 7,8 indicates the lower and higher temperatures obtained from the NIR ratio by changing the relative S/Si abundance by ±20%. As there is close agreement between the AIR-Spec temperatures and those obtained from the AIA 211/171 Å filter ratio, this shows that the S/Si relative abundance are constant with distance, as expected. In fact, the AIA temperatures are independent of the choice of abundances. If the S/Si relative abundance differed from the photospheric value by more than 20%, the NIR temperatures would differ from the AIA (and EIS) ones. The predicted radiances of the NIR lines obtained form the sperical symmetry model for the west region are also shown in Figure 2. Having established independently from the S XI the electron density, it is clear that a constant temperature model reproduces quite well the radial fall off of the NIR radiances in Si X and S XI quite well. If we used relative Si/S abundances that were not photospheric, we would find disagreement with the observed radiances.

3.4. AIA forward-model and photospheric abundances
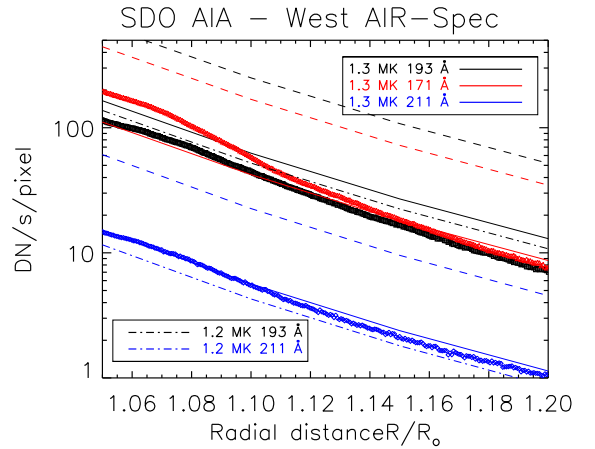
Figure 9. Measured and predicted AIA count rates in the west region. Symbols indicate the measured count rates. Solid lines show the predicted count rates using a spherical symmetry model, photospheric abundances, and assuming an isothermal and constant temperature of 1.3 MK. Dashed lines indicate the predicted signal increased by a factor of four. Dot-dashed lines show the values with the 1.2 MK isothermal model.

Having estimated the radial electron density and temperature, it is then straightforward to calculate the signal in the AIA bands using the spherical model and compare it to observation. The AIA signal depends not only on the density and temperature, but also on the absolute AIA radiometric calibration, and on the absolute iron abundance, as the AIA bands are dominated by Fe lines. In quiescent streamers, the 171 Å band is dominated by Fe IX, while the 193 band has several Fe XII and Fe XI lines. The 211 Å is mostly dominated by Fe XIII lines. The absolute AIA calibration has some uncertainty, but the degradation in these coronal bands has been relatively small (10-30%) over the years, so we do not expect an uncertainty larger than say 30%, which is the typical uncertainty in the calibration of the sounding rockets used for the in-flight calibration of AIA. Therefore, the comparison provides an estimate of the absolute iron abundance, within 30%.

Considering that a spherically-symmetric isothermal model with T=1.3 MK and the radial density profile of Del Zanna et al. (2018) represents the AIR-Spec data in the west region quite well, we have used it to calculate the AIA count rates up to 1.3 R$_\odot$. For simplicity, we have calculated only the Fe VIII – Fe XIV emissivities and folded them with the expected AIA effective areas. In fact, these are the main ions contributing to the bands. The results with photospheric abundance

are shown, together with the observed ones, in Figure 9. It is clear that there is an overall agreement, showing that such simple model can also represent the AIA observations, and that the absolute iron abundance on the west streamer must be close to photospheric. If the iron abundance were coronal, the observed count rates would be a factor of 4 higher.

The small discrepancy between the isothermal temperatures obtained from the AIA filter ratios and the assumed constant temperature of 1.3 MK is related to the fact that the ratios we have used, 193 or 211 vs. the 171 Å, provide an effective temperature weighted by the DEM distribution. If we take the predicted count rates and estimate the isothermal temperature, we get 1.2 MK from both 211/171 and 193/171 Å ratios, a value close to the peak of the DEM (1.26 MK).

Clearly, the isothermal assumption is an approximation to the real distribution, which we estimated only at 1.08 $R_\odot$ with Hinode EIS. Table 2 shows that the AIA count rates as predicted with a 1.2 and 1.3 MK isothermal models and with the EIS DEM are close, within 50%. Varying the isothermal temperature by 0.1 MK does not have a large effect on the predicted count rates, as shown in Figure 9.

Table 2. AIA observed and predicted DN/s per pixels in the west region at 1.08 $R_\odot$

	171 Å	193 Å	211 Å
Observed	103	69	8.6
Predicted (1.2 MK)	93	77	6.4
Predicted (1.3 MK)	62.	92	8.4
Predicted (DEM)	55.	57	6.2

4. CONCLUSIONS

With an improved AIR-Spec instrument, we have shown here the diagnostic potential of NIR lines to measure reliably and independently electron temperatures, densities and elemental abundances in the corona, out to large distances. For the 2019 eclipse, we could only measure lines up to 1.3 $R_\odot$, because of the limited size of the instrument and the slit, in addition to the short exposures, which were necessary to observe large sections of the corona during the eclipse. However, NIR lines, being strongly photo-excited by the disk radiation as the visible lines, have relatively strong radiances out to large distances, hence are excellent probes to study the middle corona.

The AIR-Spec results are in agreement with those obtained in the low corona by the EIS instrument. Consistency with the densities obtained from the PolarCam pB measurements and with the intensities in the SDO/AIA coronal bands is also reassuring.

In agreement with the analysis of the first 2017 AIR-Spec flight (Madsen et al. 2019), we found that the quiescent streamers have Si/S photospheric abundances, from both the AIR-Spec and the Hinode EIS lines. The spherical symmetry model which reproduces quite well the AIR-Spec data indicates that the absolute iron abundance is close to its photospheric value, by comparison with the AIA count rates. These results are also in agreement with previous literature (reviewed in the Appendix A) pointing out that the quiescent solar corona during solar minimum has near photospheric abundances, at least up to 1.3 MK.

Also, in agreement with previous observations and the 2017 AIR-Spec flight, we found that the quiescent streamer above the west limb is nearly isothermal. On the other hand, the eastern one had some hotter emission. The results from EIS, AIA and AIR-Spec are all consistent, and also in agreement with the eclipse observations in the visible. A simple spherical symmetry model with constant temperature with radial distance reproduces quite well the AIR-Spec and AIA observations, up to 1.3 $R_\odot$.

We have shown the importance of measuring at least a few key lines formed at different temperatures to establish the thermal distribution of the plasma, as we have done at lower heights with Hinode EIS. In fact, single isothermal ratios have some limitations, as they provide effective temperatures which are averaged values weighted by the DEM distribution and their temperature sensitivity.

It is also clear that the analysis of NIR lines is non-trivial as careful atmospheric modeling is required, as well as a model of the electron density and temperature distribution, as the radiances cannot be directly used to measure these parameters. This is because of the variable contribution of the resonantly scattered component to the line emission, compared to the collisionally excited one. Once the electron density is established, it is relatively easy to find a temperature distribution that fits the observations. Therefore, we recommend that future NIR observations include at least a density-sensitive line ratio such as the S XI, and at least three lines formed in the temperature range between 1 and 2 MK for the quiet corona.

As briefly described in Del Zanna & DeLuca (2018), the NIR spectral region is virtually unexplored but has a great plasma diagnostic potential. The follow-up to

AIR-Spec is the Airborne Coronal Emission Surveyor (ACES), a new imaging Fourier transform spectrometer that will survey the entire 1–4 µm spectral range at high (0.5 cm^{-1}) spectral resolution during the April 8, 2024 total solar eclipse. ACES will fly along the path of totality on the GV, with a 20 cm solar feed stabilized to 6″ RMS over one second. The feed will be provided by the Airborne Stabilized Platform for InfraRed Experiments (ASPIRE), which was developed by the AIR-Spec/ACES team for the GV and commissioned in 2021. ACES will measure many coronal lines, half of which have never been observed before, and will therefore be a pathfinder for future targeted DKIST and hopefully space-based observations.

REFERENCES

Andretta, V., & Del Zanna, G. 2014, A&A, 563, A26, doi: 10.1051/0004-6361/201322841

Asplund, M., Grevesse, N., Sauval, A. J., & Scott, P. 2009, ARA&A, 47, 481, doi: 10.1146/annurev.astro.46.060407.145222

Boe, B., Habbal, S., Downs, C., & Druckmüller, M. 2022, ApJ, 935, 173, doi: 10.3847/1538-4357/ac8101

Culhane, J. L., Harra, L. K., James, A. M., et al. 2007, SoPh, 60, doi: 10.1007/s01007-007-0293-1

Del Zanna, G. 2012, A&A, 537, A38, doi: 10.1051/0004-6361/201117592

Del Zanna, G. 2013a, A&A, 555, A47, doi: 10.1051/0004-6361/201220810

—. 2013b, A&A, 558, A73, doi: 10.1051/0004-6361/201321653

Del Zanna, G. 2019, A&A, 624, A36, doi: 10.1051/0004-6361/201834842

Del Zanna, G., & Andretta, V. 2011, A&A, 528, A139+, doi: 10.1051/0004-6361/201016106

Del Zanna, G., Berrington, K. A., & Mason, H. E. 2004, A&A, 422, 731, doi: 10.1051/0004-6361:20034432

Del Zanna, G., & Bromage, B. J. I. 1999, J. Geophys. Res., 104, 9753. http://cdsads.u-strasbg.fr/cgi-bin/nph-bib_query?bibcode=1999JGR...104.9753D&db_key=AST

Del Zanna, G., & DeLuca, E. E. 2018, ApJ, 852, 52, doi: 10.3847/1538-4357/aa9edf

Del Zanna, G., Dere, K. P., Young, P. R., & Landi, E. 2021, ApJ, 909, 38, doi: 10.3847/1538-4357/abd8ce

Del Zanna, G., Dere, K. P., Young, P. R., Landi, E., & Mason, H. E. 2015, A&A, 582, A56, doi: 10.1051/0004-6361/201526827

Del Zanna, G., Gupta, G. R., & Mason, H. E. 2019, A&A, 631, A163, doi: 10.1051/0004-6361/201834625

Del Zanna, G., Landini, M., & Mason, H. E. 2002, A&A, 385, 968, doi: 10.1051/0004-6361:20020164

Del Zanna, G., & Mason, H. E. 2014, A&A, 565, A14, doi: 10.1051/0004-6361/201423471

—. 2018, Living Reviews in Solar Physics, 15

Del Zanna, G., O'Dwyer, B., & Mason, H. E. 2011, A&A, 535, A46, doi: 10.1051/0004-6361/201117470

Del Zanna, G., Raymond, J., Andretta, V., Telloni, D., & Golub, L. 2018, ApJ, 865, 132, doi: 10.3847/1538-4357/aadcf1

Del Zanna, G., Rozum, I., & Badnell, N. R. 2008, A&A, 487, 1203, doi: 10.1051/0004-6361:200809998

Del Zanna, G., Mondal, B., Rao, Y. K., et al. 2022, ApJ, 934, 159, doi: 10.3847/1538-4357/ac7a9a

Ding, A., & Habbal, S. R. 2017, ApJL, 842, L7, doi: 10.3847/2041-8213/aa7460

Doschek, G. A., Laming, J. M., Feldman, U., et al. 1998, ApJ, 504, 573, doi: 10.1086/306043

Doschek, G. A., & Warren, H. P. 2019, ApJ, 884, 158, doi: 10.3847/1538-4357/ab426e

Dudík, J., Del Zanna, G., Rybák, J., et al. 2021, ApJ, 906, 118, doi: 10.3847/1538-4357/abcd91

Feldman, U. 1992, PhyS, 46, 202

Feldman, U., Doschek, G. A., Schühle, U., & Wilhelm, K. 1999, ApJ, 518, 500, doi: 10.1086/307252

Feldman, U., Mandelbaum, P., Seely, J. F., Doschek, G. A., & Gursky, H. 1992, ApJS, 81, 387

Feldman, U., Schühle, U., Widing, K. G., & Laming, J. M. 1998, ApJ, 505, 999, doi: 10.1086/306195

Feldman, U., & Widing, K. G. 1993, ApJ, 414, 381, doi: 10.1086/173084

Fineschi, S., Gardner, L. D., Kohl, J. L., Romoli, M., & Noci, G. C. 1998, in Society of Photo-Optical Instrumentation Engineers (SPIE) Conference Series, Vol. 3443, X-Ray and Ultraviolet Spectroscopy and Polarimetry II, ed. S. Fineschi, 67–74, doi: 10.1117/12.333614

Habbal, S. R., Druckmüller, M., Morgan, H., et al. 2011, The Astrophysical Journal, 734, 120, doi: 10.1088/0004-637x/734/2/120

Habbal, S. R., Druckmüller, M., Alzate, N., et al. 2021, ApJL, 911, L4, doi: 10.3847/2041-8213/abe775

Hanaoka, Y., Sakai, Y., & Takahashi, K. 2021, SoPh, 296, 158, doi: 10.1007/s11207-021-01907-0

Jordan, C. 1971, SoPh, 21, 381, doi: 10.1007/BF00154289

Judge, P., Casini, R., Tomczyk, S., Edwards, D. P., & Francis, E. 2001, Coronal Magnetogmetry: A feasibility study, Tech. Rep. NCAR/TN-446-STR, National Center for Atmospheric Research, doi: 10.5065/D6222RQH

Judge, P., Berkey, B., Boll, A., et al. 2019, SoPh, 294, 166, doi: 10.1007/s11207-019-1550-3

Judge, P. G. 1998, The Astrophysical Journal, 500, 1009, doi: 10.1086/305775

Koutchmy, S., Baudin, F., Abdi, S., Golub, L., & Sèvre, F. 2019, A&A, 632, A86, doi: 10.1051/0004-6361/201935681

Laming, J. M. 2015, Living Reviews in Solar Physics, 12, 2, doi: 10.1007/lrsp-2015-2

Laming, J. M., Drake, J. J., & Widing, K. G. 1995, ApJ, 443, 416, doi: 10.1086/175534

Laming, J. M., Vourlidas, A., Korendyke, C., et al. 2019, ApJ, 879, 124, doi: 10.3847/1538-4357/ab23f1

Landi, E., Habbal, S. R., & Tomczyk, S. 2016, Journal of Geophysical Research (Space Physics), 121, 8237, doi: 10.1002/2016JA022598

Madsen, C. A., Samra, J. E., Del Zanna, G., & DeLuca, E. E. 2019, ApJ, 880, 102, doi: 10.3847/1538-4357/ab2b3c

Malinovsky, L., & Heroux, M. 1973, ApJ, 181, 1009

Mariska, J. T., & Withbroe, G. L. 1978, SoPh, 60, 67, doi: 10.1007/BF00152333

Reames, D. V. 2018, SoPh, 293, 47, doi: 10.1007/s11207-018-1267-8

Rimmele, T. R., Warner, M., Keil, S. L., et al. 2020, SoPh, 295, 172, doi: 10.1007/s11207-020-01736-7

Samra, J. E., Judge, P. G., DeLuca, E. E., & Hannigan, J. W. 2018, The Astrophysical Journal Letters, 856, L29. https://doi.org/10.3847/2041-8213/aab434

Samra, J. E., Judge, P. G., DeLuca, E. E., & Hannigan, J. W. 2019, ApJL, 873, L25, doi: 10.3847/2041-8213/ab0ae0

Samra, J. E., Madsen, C. A., Cheimets, P., et al. 2022, ApJ, 933, 82, doi: 10.3847/1538-4357/ac6ce8

Samra, J. E., Marquez, V., Cheimets, P., et al. 2022, The Astronomical Journal, 164, 39, doi: 10.3847/1538-3881/ac7218

Tomczyk, S., & Landi, E. 2019, in Solar Heliospheric and INterplanetary Environment (SHINE 2019), 131

Tomczyk, S., Landi, E., Berkey, B., et al. 2021, in AGU Fall Meeting Abstracts, Vol. 2021, 2089

Tritschler, A., Rimmele, T. R., Berukoff, S., et al. 2016, Astronomische Nachrichten, 337, 1064, doi: 10.1002/asna.201612434

Vadawale, S. V., Mondal, B., Mithun, N. P. S., et al. 2021, The Astrophysical Journal Letters, 912, L12, doi: 10.3847/2041-8213/abf35d

van de Hulst, H. C. 1950, BAN, 11, 135

Warren, H. P., Ugarte-Urra, I., & Landi, E. 2014, ApJS, 213, 11, doi: 10.1088/0067-0049/213/1/11

Watts, C. B. 1963, Astron. Papers Am. Ephemeris, XVII

West, M. J., Seaton, D. B., Wexler, D. B., et al. 2022, arXiv e-prints, arXiv:2208.04485. https://arxiv.org/abs/2208.04485

Withbroe, G. 1991, Advances in Space Research, 11, 5, doi: 10.1016/0273-1177(91)90083-V

Yang, Z., Bethge, C., Tian, H., et al. 2020, Science, 369, 694, doi: 10.1126/science.abb4462

Young, P. R. 2005, A&A, 439, 361, doi: 10.1051/0004-6361:20052963

APPENDIX

A. ELEMENTAL ABUNDANCES IN THE QUIET SUN

Solar coronal abundances measured with remote-sensing instruments vary with the structure observed and the temperature of formation of the spectral lines observed. For a review of measurements of different solar features we refer to Del Zanna & Mason (2018). Historically, most observations have constrained the relative abundances between high- (e.g. Ne, O, Ar) and low-FIP (e.g. Si, Fe, Mg) elements, and take the ratio with the photospheric ones to obtain the FIP bias. We adopt here the photospheric abundances of Asplund et al. (2009), but note that the values for several elements (especially C, N, O) are still debated in the literature, although variations from Asplund et al. are of the order of 30%. We also note that the Ne, Ar abundances recommended by Asplund et al. (2009) are not based on actual photospheric measurements.

We focus here on 'quiet Sun' (QS) areas during solar minimum, and note that the presence of active regions has a significant effect on the diffuse QS emission, as shown e.g. in Del Zanna & Andretta (2011); Andretta & Del Zanna (2014).

Early QS observations from Skylab in transition-region lines indicated near photospheric relative abundances, when considering Mg/Ne ratios (see, e.g. Feldman 1992; Feldman & Widing 1993, and references therein). Similar results were obtained with SoHO CDS, also considering Mg/Ne ratios (see, e.g. Del Zanna & Bromage 1999; Young 2005).

SoHO SUMER was an excellent instrument to measure the relative abundances of coronal lines in off-limb QS regions. Doschek et al. (1998) used SOHO SUMER observations to find photospheric Si/Ne abundances in the upper transition region. Other results involving more elements were unclear, as they depended on which spectral lines were considered, as discussed by Feldman et al. (1998). The problem was partly related to the inclusion or not of lines from the so-called 'anomalous' ions of the Li-like and Na-like isoelectronic sequences (see e.g. Del Zanna et al. 2002, and references therein).

We note that the atomic data for the forbidden lines of Fe ions in the SUMER spectra were significantly revised by one of us (GDZ), as summarised in Del Zanna & Mason (2018). The new atomic data were included in CHIANTI version 8 (Del Zanna et al. 2015). A reanalysis of the SUMER observations with these updated atomic data have indicated relative photospheric abundances, considering a range of low-FIP elements such as Fe, high-FIP ones such as Ne, O, and Ar, and the mid-FIP S (Del Zanna & DeLuca 2018).

The SUMER off-limb spectra were also used by Feldman et al. (1998) to find an O/H ratio to be close to the photospheric value.

Hinode EIS has been used extensively in the literature to measure the FIP bias. The instrument observes strong coronal lines from Fe and Si (low-FIP), but much weaker lines from S and Ar. In most observations, only a weak Ar XIV can reliably provide the Fe,Si vs. Ar relative abundance in 3 MK plasma, found in the cores of active regions. The results are that the FIP bias is always about a factor of 3, as in the example shown in Del Zanna (2013b). This agrees with an analysis of many quiescent active region cores observed in the X-rays, where the Fe vs. O, Ne FIP bias is also about 3 (Del Zanna & Mason 2014), i.e. lower than 4, the earlier widely adopted value recommended by Feldman et al. (1992).

The Hinode EIS observations of S XIII, also formed around 3 MK, confirm an Fe, Si vs. S FIP bias of about 3 (Del Zanna 2013b) (while the lower charge states of S often indicate a lower FIP bias of about 2). Therefore, S in remote-sensing observations shows the same FIP bias as the high-FIP elements O, Ne, so effectively behaves as a high-FIP element, despite having a FIP of only 10 eV. The behaviour of S as a high-FIP element is also observed in solar energetic particles (SEP) events measured in-situ, and predicted by Laming's theory (see, e.g. Reames 2018; Laming et al. 2019). It is also interesting to note that the FIP bias of SEP is about 3, in agreement with the recent results for active region cores.

On the basis of the above arguments, there is an extended literature on FIP bias results obtained from Hinode EIS measurements of the strong S X vs. Si X lines around 264 Å, as they are formed at similar temperatures (which depend on the feature observed), and are close in wavelength (so the uncertainty in the radiometric calibration is small). When observing the QS, the S X always indicates a relative Si, Fe vs. S photospheric abundance, while active regions show a FIP bias of around 2 (see,e.g. Del Zanna 2012; Doschek & Warren 2019).

The AIR-Spec NIR spectra of the 2017 eclipse, when the Sun was very quiet, have also indicated a photospheric S/Si abundance (Madsen et al. 2019).

It could well be that QS plasma at temperatures higher than 1 MK has a FIP bias, but past/current instrumentation is not sensitive enough to measure it. Strong lines from low-FIP elements formed around 2 MK are usually very weak, and lines formed around 3 MK have no signal in past and current instrumentation. Spectral lines from high-FIP formed around 2 MK or more have no signal in the quiet Sun.

Regarding absolute abundances, in earlier literature it was not clear if it was the low-FIP elements that were more abundant in active regions, or the high-FIP ones that were less abundant. Line to continuum measurements during large flares, when the FIP bias is generally 1, indicated photospheric abundances for all the elements. Regarding quiescent active cores, on the basis of a filling factor argument, Del Zanna (2013b) suggested that it should be the low-FIP elements that have increased abundances. Line-to continuum measurements in the X-rays of the full Sun, when a single active region was dominating the signal, indicated a Si FIP bias of 2.4 (Del Zanna et al. 2022), i.e. only about 20% lower than the value suggested by Del Zanna.

Irradiance measurements (i.e. Sun-as-a-star) have been carried out since the 1960's in the X-rays and EUV. Most measurements were carried out outside of solar minimum, hence the presence of active regions affected the results in terms of elemental abundances. One example is the 1969 sounding rocket flight described by Malinovsky & Heroux (1973). It obtained the best-calibrated EUV spectrum of the Sun, but active region lines (formed above 2 MK) and even flare lines were present. Laming et al. (1995) used that spectrum to find nearly photospheric abundances when considering lines formed in the transition region and corona, up to 1 MK. The abundances were relative, using mainly sulphur lines, in combination with lines from low-FIP elements. An FIP bias of 3–4 was instead obtained from higher-temperature lines. A re-analysis of the same spectrum by Del Zanna (2019) using CHIANTI version 8 found similar results, showing no FIP bias when considering S X, and an increase to a FIP bias of about 2 when considering S XI and S XII, formed around 2 MK. As explained by Del Zanna (2019), this difference is simply due to the fact that the QS dominates the S X emission (hence the FIP bias is 1), while active regions dominate the S XI, S XII, hence the increase in the FIP bias. Finally, we note that X-ray bright points also contribute to the irradiances at 2 MK with an FIP bias of about 2, as found from line to continuum measurements in the X-rays (Vadawale et al. 2021).

On the other hand, when analysing irradiances during solar minimum, the relative abundance between sulphur lines and those of low-FIP elements is photospheric, as shown by Del Zanna (2019) using the well-calibrated spectra measured during the solar minimum on 2008 April 14 by the prototype of the Solar Dynamics Observatory Extreme ultraviolet Variability Experiment (EVE).

B. NEAR-ISOTHERMAL AND CONSTANT ELECTRON TEMPERATURE IN QUIESCENT STREAMERS

As reviewed in Del Zanna & Mason (2018), measuring the electron temperature directly from e.g. line ratios is possible but was rarely applied to observations, in particular those of the quiet Sun corona above the limb, as its temperature is about 1 MK and very few diagnostics are available.

The best one is a line ratio from Mg IX. Del Zanna et al. (2008) produced significantly improved atomic data for this ion, and used off-limb SoHO SUMER measurements reported by Feldman et al. (1999) to find a temperature of 1.35 MK.

Another possible diagnostic, applied to a quiescent streamer at a large distance $(2.7\,\mathrm{R_\odot})$, involved measuring the extremely weak electron-scattered component of the neutral hydrogen Ly α as recorded by SoHO UVCS (Fineschi et al. 1998). A temperature of 1.1 ± 0.3 MK was found.

Lacking direct diagnostics, the usual assumption to estimate the electron temperature is to measure the ionization temperature, i.e. the temperature obtained with line ratios or emission measure analyses, assuming ionization equilibrium. Early measurements of line ratios from the 1970's of the inner corona of the quiet Sun have indicated a temperature distribution around 1.4 MK (cf. Jordan 1971).

Detailed emission measure analyses obtained with a range of coronal lines observed by SoHO SUMER clearly indicated an isothermal distribution along the line of sight for QS off-limb regions (Feldman et al. 1999). A reanalysis of the same SUMER observations with improved atomic data, shown in Del Zanna & Mason (2018), confirms this result, with a temperature of 1.35 MK, in exact agreement with the Mg IX result. This provides a strong indication that for the QS the ionization temperature is a good measure of the electron temperature, and that the CHIANTI atomic data, in particular the ionization/recombination rates for the ions considered, are accurate.

There is also evidence in the literature that the temperature is relatively constant with radial distance, if one observes quiescent streamers, when no active regions are present. For example, Skylab ATM observations of EUV coronal lines out to $1.25\,\mathrm{R}_\odot$ indicated a nearly constant ionization temperature (Mariska & Withbroe 1978). SoHO UVCS observations of EUV coronal lines in quiescent streamers, between 1.4 and 3 $\mathrm{R}_\odot$, also indicated a constant ionization temperature of about 1.4 MK (Del Zanna et al. 2018). Clearly, close to the solar limb the temperature decreases towards lower values. Semi-empirical models of the electron temperature in quiescent streamers also indicated nearly constant values (see, e.g. Withbroe 1991). Finally, narrow-band images in iron visible lines during eclipses also indicate a nearly constant ionization temperature (see, e.g. Boe et al. 2022).

C. MEASURING DENSITY AND TEMPERATURE USING IR LINE RATIOS

The mapping from AIR-Spec line ratios to electron density was provided by the 'DENSITY_RATIOS' routine in CHIANTI v.10 (Del Zanna et al. 2021). As the IR lines are significantly photo-excited, the distance from the underlying photospheric radiation field is a critical parameter in the mapping: as the radiation becomes diluted with increasing distance, the pumping rate also decreases. Figure 10 shows the dependence of density on the combination of the S XI 1.92/1.39 µm line ratio and the distance from Sun center. The AIR-Spec density estimates were computed by interpolating the density surface in Figure 10 to each line ratio/radial distance pair in the AIR-Spec data. This procedure produces the density estimates in the left half of Figure 5, which are not corrected for LOS contributions to the AIR-Spec radiances.
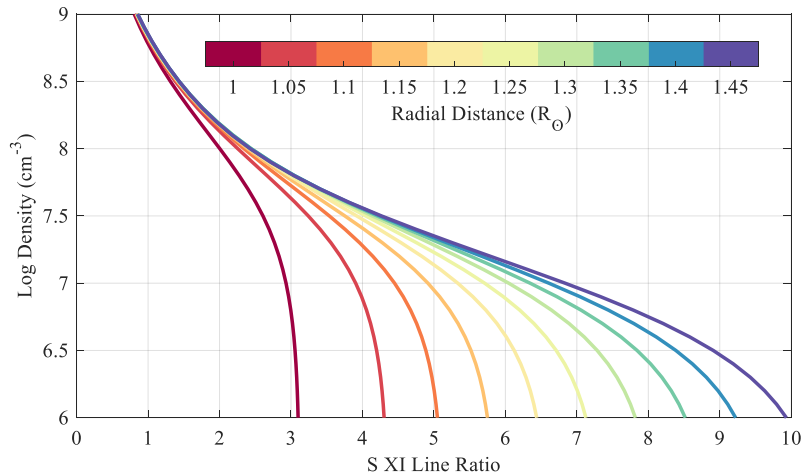
Figure 10. Density as a function of S XI 1.92/1.39 µm line ratio and distance from Sun center.

In order to estimate the radial (LOS-corrected) density profile, we use the spherically symmetric model described in Del Zanna et al. (2018) to remove the AIR-Spec intensity contribution from outside the plane of the sky (POS). Figure 11 shows the fraction of the total line intensity contributed by each **0.025 $\mathrm{R}_\odot$** along the LOS, as predicted by the model. Only 4–5% of the contribution comes from the **0.025 $\mathrm{R}_\odot$** nearest the POS. If we scale the AIR-Spec S XI intensities by this fraction before taking the line ratio, we obtain the radial density estimates in the right half of Figure 5.

Figure 12 shows the emissivities (contribution functions, calculated in ionization equilibrium) of the main AIR-Spec lines, indicating the range of temperatures where the lines can be formed. We use the emissivity ratio of the two strongest lines, Si X 1.43 µm and S XI 1.92 µm, to estimate the temperatures shown in Figures 7c and 8. The contribution functions are computed using photoexcitation and integrated along the LOS before the ratio is taken. Because the modeled line ratio includes emission from the entire LOS, the LOS-averaged AIR-Spec radiances are used to map line ratio to temperature.

As with the density mapping, the distance from the underlying photospheric radiation field is an important parameter in the mapping from line ratio to temperature. Figure 13 shows the dependence of temperature on the combination of the Si X 1.43 µm/S XI 1.92 µm line ratio and the distance from Sun center. The line ratio is sensitive to temperatures in the 1–2 MK range.
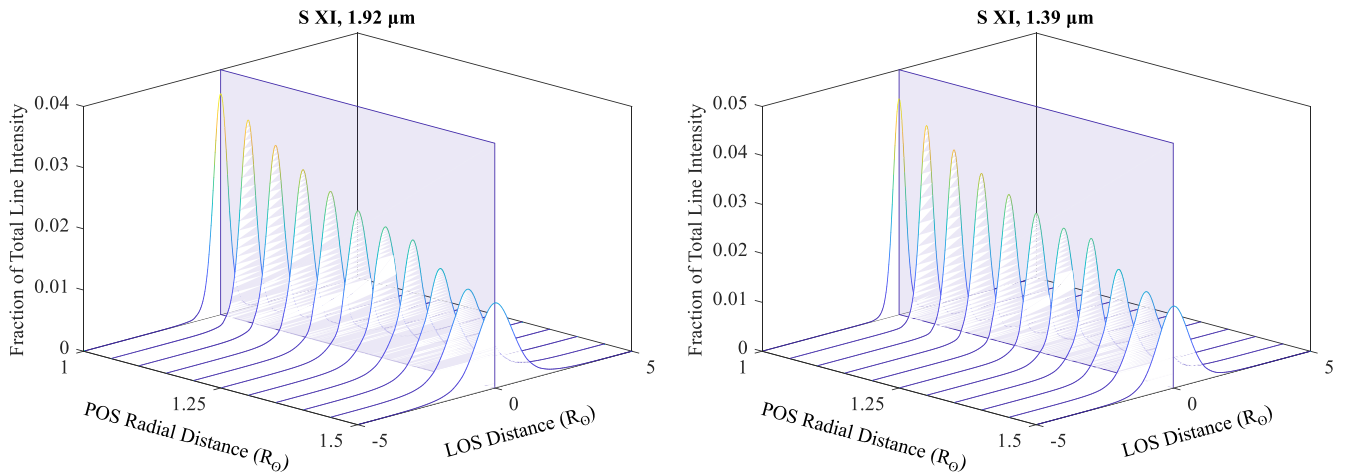
Figure 11. Fraction of line intensity contributed by each 0.025 $R_\odot$ along the line of sight. Each curve sums to one along the 'LOS Distance' coordinate. The 1.92 µm line has a smaller contribution from the POS than the 1.39 µm line, resulting in a lower line ratio (and higher density) when only the POS intensity is taken into account instead of the entire LOS integration.
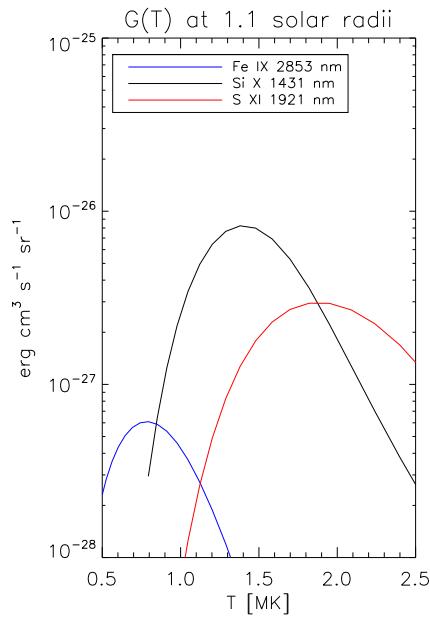
Figure 12. Contribution functions of the main AIR-Spec lines, calculated with photoexcitation at $1.1\,R_\odot$.

D. TEMPERATURE DISTRIBUTION FROM EIS

Figure 14 shows the averaged EIS spectra in the east and west regions, used to obtain the DEM distribution. The strongest lines are from Fe X–Fe XIII, and Si X. The west region has significant emission in Fe XIV and Fe XV which is not present on the east. The S X lines are well observed and provide a strong constraint on the relative FIP bias between high-FIP and low-FIP elements.

Table 3 shows the results of the DEM analysis on the off-limb observation above the east limb. Only a few of the lines are shown. $T_{\max}$ is the temperature of the maximum of the contribution function $G(T)$, while the effective temperature T_{eff} is:

$$T_{\mathrm{eff}} = \int G(T)\, DEM(T)\, T\, dT / \int G(T)\, DEM(T)\, dT \quad . \tag{D1}$$
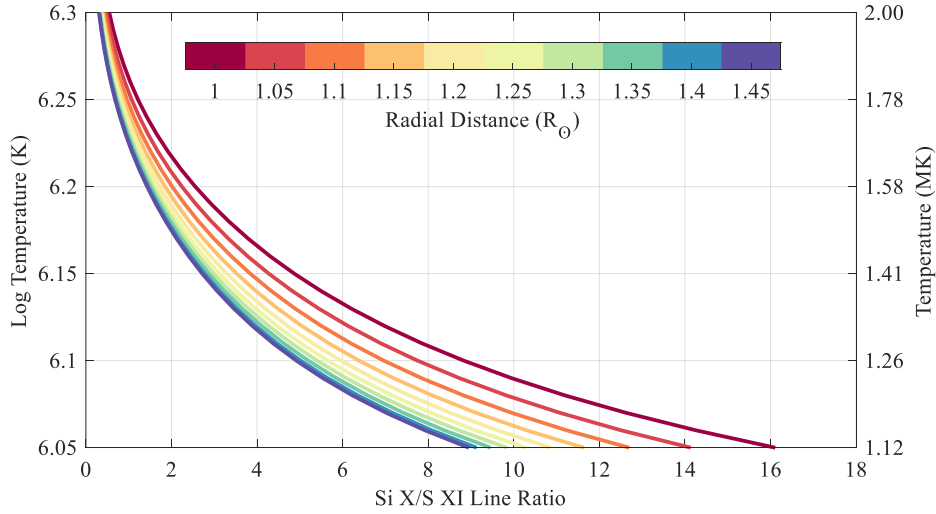
Figure 13. Temperature as a function of Si X/S XI 1.43/1.92 µm line ratio and distance from Sun center.

For each observed line, the CHIANTI programs search for all the transitions (that form a blend) within a wavelength range, centred on the observed wavelength. Only the main lines contributing to the blend are listed, with their fractional contribution indicated in the last column. Table 4 shows the results of the DEM analysis on the off-limb observation above the west limb. Only a few of the lines are shown.

E. EIS CALIBRATION

We performed a DEM analysis of a quiet Sun off-limb observations close in time to the eclipse, on 2019- 06-28 at 09:38 UT, with the 2″ slit and 60 s exposures. Table 5 gives a list of the main lines. The emissivities were calculated at a constant density log Ne =8.6. The EIS effective areas were adjusted to match observation. This calibration was then used for the Eclipse observations. It is clear that all the main lines are well represented within ±15%.

Figure 15 shows the emissivity ratios of a selection of lines, from four of the main ions observed by EIS. The emissivity ratios are essentially the ratios of the observed intensities vs. the theoretical ones, as a function of density, calculated for a constant temperature (see Del Zanna et al. 2004). It is clear that the main density-diagnostic ratios from Fe XII, Fe XIII, and Si X give consistent densities. Note that the main Fe XII lines, at 192,193,195 Å are somewhat affected by opacity (i.e. their observed intensities are lower than expected), a typical feature of active region and off-limb observations, as shown for the first time by Del Zanna et al. (2019).

F. EIS/AIA CO-ALIGNMENT

We took the AIA observations during the EIS rasters, and compared them with the predicted AIA DN/s in the EIS FOV, using the updated EIS calibration. We reduced the AIA count rates to the EIS spatial resolution, and assumed a slit step size of 1.9″. The results are shown in Figure 17. The EIS jittering, bias and point spread function limit the accuracy of the comparison. As the radial decrease in the signal is very steep, we can accurately estimate the EIS pointing in the E-W direction (to within 2–4″), while the N-S pointing is more uncertain (5–10″).

G. EIS DENSITIES ON ECLIPSE DAY

Figure 18 shows the Electron densities obtained from a selection of EIS line ratios on the west and east regions. The uncertainties are obtained by assuming a ±15 % uncertainty on the observed ratios, projected onto the theoretical variation of the ratio, to obtain a lower and upper limit, shown in the plot. The 15 % is a reasonable estimate of the uncertainty due to the radiometric calibration, which is the main uncertainty. There is generally good agreement among the three line ratios, especially on the west region.
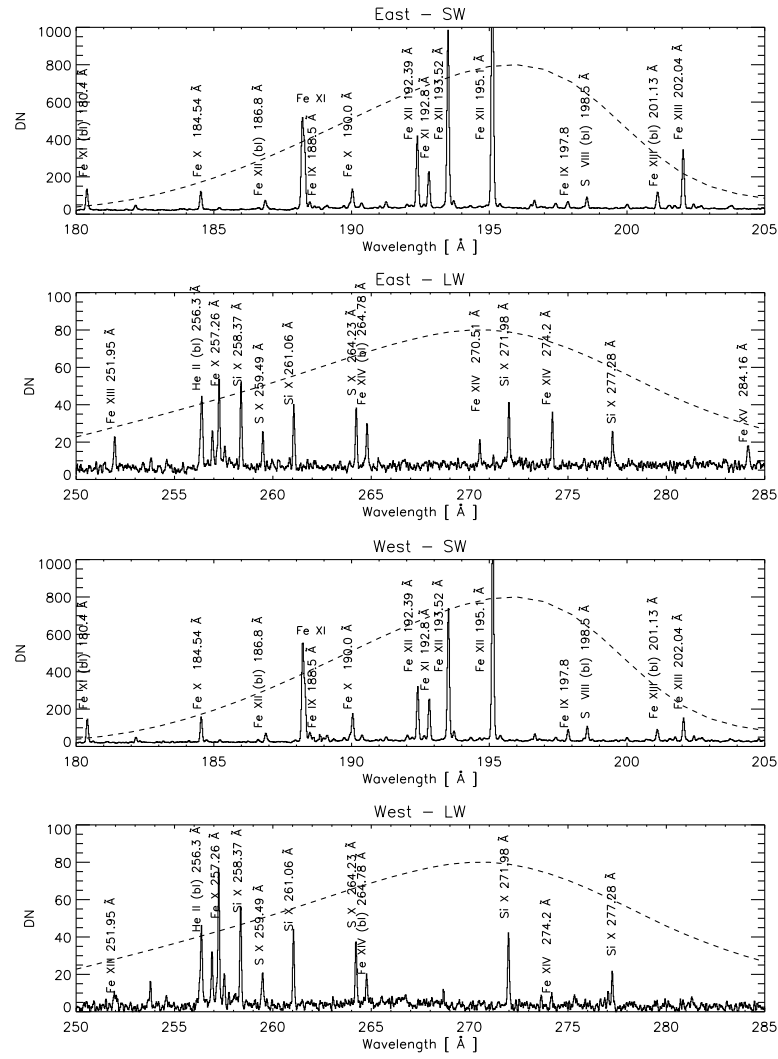
Figure 14. Hinode EIS spectra for the off-limb observation above the east and west limb (120 s, 2″ slit), around 1.09 R⊙. The dashed lines are the scaled ground-calibration effective area, to show why spectral lines in the middle of the two SW and LW detectors are stronger.

Table 3. Observed and predicted radiances for the off-limb observation above the east limb (120 s, 2″ slit). λ_{obs} (Å) are the observed wavelengths, DN is the number of total counts in each line, while I_{obs} is the calibrated radiance (erg cm^{-2} s^{-1} sr^{-1}) obtained with our new EIS calibration. T_{max} and T_{eff} are the maximum and effective temperature (log values, in K; see text), R the ratio between the predicted and observed radiances, Ion and λ_{exp} (Å) the main contributing ion, and r the fractional contribution to the blend.

λ_{obs}	DN	I_{obs}	$\log T_{\mathrm{max}}$	$\log T_{\mathrm{eff}}$	R	Ion	λ_{exp}	r
185.20	47	5.6	5.73	6.06	0.83	Fe VIII	185.213	0.94
186.61	57	4.7	5.72	6.06	0.84	Fe VIII	186.598	0.81
189.93	80	3.5	5.92	6.10	1.10	Fe IX	189.935	0.95
188.48	142	8.9	5.93	6.10	1.06	Mn IX	188.480	0.11
						Fe IX	188.493	0.83
197.85	128	3.8	5.93	6.10	1.15	Fe IX	197.854	0.93
257.27	213	41.6	6.02	6.11	0.98	Fe X	257.259	0.21
						Fe X	257.261	0.77
184.53	403	56.4	6.03	6.12	0.80	Fe X	184.537	0.96
190.03	391	16.5	6.03	6.12	1.00	Fe X	190.037	0.86
198.54	236	7.2	5.95	6.12	1.45	S VIII	198.553	0.44
						Fe XI	198.538	0.51
192.81	811	26.3	5.42	6.13	1.15	Fe XI	192.813	0.97
188.21	1940	131.0	6.12	6.14	1.10	Fe XI	188.216	0.98
188.29	1370	90.2	6.12	6.14	0.98	Fe XI	188.299	0.98
180.39	475	337.0	6.12	6.14	0.90	Fe XI	180.401	0.98
258.38	201	37.7	6.15	6.14	1.03	Si X	258.374	0.97
272.00	151	20.1	6.15	6.14	1.00	Si X	271.992	0.98
261.07	137	21.9	6.15	6.14	1.12	Si X	261.056	0.98
277.27	73	14.9	6.15	6.14	1.04	Si X	277.264	0.98
259.49	80	14.4	6.18	6.15	1.01	S X	259.496	0.98
264.24	133	18.7	6.18	6.15	1.13	S X	264.230	0.98
193.50	3860	117.0	6.19	6.15	1.10	Fe XII	193.509	0.94
195.11	6460	169.0	6.19	6.15	1.09	Fe XII	195.119	0.97
192.39	1580	54.7	6.19	6.15	1.08	Fe XII	192.394	0.97
200.01	113	4.1	6.24	6.17	1.14	Fe XIII	200.021	0.91
191.25	124	4.8	6.28	6.17	1.03	S XI	191.266	0.94
251.97	67	21.3	6.24	6.17	1.05	Fe XIII	251.952	0.97
202.04	1260	113.0	6.24	6.17	0.86	Fe XIII	202.044	0.97
264.79	94	13.2	6.29	6.17	1.20	Fe XIV	264.788	0.61
						Fe XI	264.772	0.36
274.21	125	17.9	6.29	6.19	0.86	Fe XIV	274.203	0.95
270.52	57	8.1	6.29	6.19	0.82	Fe XIV	270.520	0.97
262.98	4	0.61	6.43	6.20	1.16	Fe XVI	262.976	0.26
						Fe XIII	262.984	0.66
284.16	47	20.5	6.34	6.22	1.05	Fe XV	284.163	0.96

Table 4. Observed and predicted radiances for the off-limb observation above the west limb (120 s, 2″ slit). The notation is the same as Table 3.

λ_{obs}	DN	I_{obs}	$\log T_{\max}$	$\log T_{\mathrm{eff}}$	R	Ion	$\lambda_{\exp}$	r
185.22	48	5.8	5.73	6.07	1.08	Fe VIII	185.213	0.97
189.94	109	4.7	5.92	6.08	1.08	Fe IX	189.935	0.98
197.86	231	6.9	5.93	6.08	0.92	Fe IX	197.854	0.95
257.25	312	61.1	6.02	6.09	0.88	Fe X	257.259	0.20
						Fe X	257.261	0.78
184.54	538	75.3	6.03	6.09	0.75	Fe X	184.537	0.97
190.04	575	24.3	6.03	6.09	0.83	Fe X	190.037	0.90
198.56	293	9.0	5.95	6.09	1.26	S VIII	198.553	0.54
						Fe XI	198.538	0.42
256.91	117	23.2	6.10	6.09	0.96	Fe XI	256.919	0.98
180.41	513	364.0	6.11	6.10	0.83	Fe XI	180.401	0.93
188.22	2040	137.0	6.12	6.10	0.99	Fe XI	188.216	0.98
192.82	877	28.4	6.12	6.10	1.01	Fe XI	192.813	0.97
256.37	223	46.1	6.16	6.10	0.81	Si X	256.377	0.65
						Fe XII	256.410	0.14
						Fe X	256.398	0.12
258.36	219	41.2	6.15	6.10	0.72	Si X	258.374	0.97
271.98	173	23.0	6.15	6.10	0.73	Si X	271.992	0.98
261.05	166	26.6	6.15	6.10	0.76	Si X	261.056	0.98
264.22	140	19.7	6.18	6.10	0.80	S X	264.230	0.98
193.52	2850	86.2	6.19	6.10	0.99	Fe XII	193.509	0.94
192.40	1100	38.1	6.19	6.10	1.02	Fe XII	192.394	0.97
195.13	4660	122.0	6.19	6.10	0.99	Fe XII	195.119	0.97
264.77	63	8.8	6.29	6.11	0.88	Fe XIV	264.788	0.26
						Fe XI	264.772	0.71
200.00	62	2.3	6.24	6.11	0.70	Fe XIII	200.021	0.81
191.26	61	2.4	6.28	6.11	0.95	S XI	191.266	0.91
202.05	471	42.2	6.24	6.12	0.96	Fe XIII	202.044	0.97
274.17	22	3.3	6.29	6.13	1.09	Fe XIV	274.203	0.89
						Fe XI	256.654	0.18

DEL ZANNA ET AL.

Table 5. Observed and predicted radiances for the off-limb observation (60s, 2″ slit) on 2019-Jun-28 used for the EIS radiometric calibration. The notation is the same as Table 3.

λ_{obs}	DN	I_{obs}	$T_{\max}$	T_{eff}	R	Ion	$\lambda_{\exp}$	r
194.66	417	22.6	5.72	6.05	1.04	Fe VIII	194.661	0.95
185.22	412	97.0	5.73	6.05	1.17	Fe VIII	185.213	0.96
186.60	464	75.6	5.73	6.06	1.17	Fe VIII	186.598	0.85
189.94	785	67.4	5.94	6.08	1.23	Fe IX	189.935	0.97
188.49	1290	162.0	5.95	6.08	1.00	Fe IX	188.493	0.89
197.85	1320	78.9	5.96	6.09	1.04	Fe IX	197.854	0.94
257.26	1510	589.0	6.04	6.10	0.95	Fe X	257.259	0.25
						Fe X	257.263	0.73
177.24	346	1650.0	6.05	6.11	1.08	Fe X	177.240	0.98
174.53	177	2660.0	6.05	6.11	1.19	Fe X	174.531	0.98
184.54	2280	637.0	6.05	6.11	1.06	Fe X	184.537	0.96
190.04	3050	257.0	6.06	6.12	1.09	Fe XII	190.040	0.12
						Fe X	190.037	0.76
184.79	164	43.3	6.12	6.13	1.20	Fe XI	184.793	0.93
257.55	441	170.0	6.12	6.13	1.07	Fe XI	257.554	0.70
						Fe XI	257.547	0.25
189.02	427	47.3	6.13	6.13	0.87	Fe XI	188.997	0.95
256.92	608	241.0	6.12	6.13	0.86	Fe XI	256.919	0.92
181.13	150	167.0	6.13	6.13	0.89	Fe XI	181.130	0.97
192.81	5040	326.0	5.42	6.13	0.91	Fe XI	192.813	0.96
188.22	9190	1240.0	6.13	6.13	1.13	Fe XI	188.216	0.98
188.30	6090	801.0	6.13	6.13	1.06	Fe XI	188.299	0.98
180.40	1820	2570.0	6.13	6.13	1.13	Fe XI	180.401	0.98
202.71	424	87.6	6.13	6.14	1.37	Fe XI	202.705	0.93
258.37	1460	546.0	6.15	6.14	0.96	Si X	258.374	0.97
253.79	223	115.0	6.15	6.14	0.90	Si X	253.790	0.97
271.99	852	226.0	6.15	6.14	0.93	Si X	271.992	0.97
261.06	853	273.0	6.15	6.14	0.92	Si X	261.056	0.98
277.27	452	181.0	6.15	6.14	0.89	Si X	277.264	0.98
249.39	107	89.1	6.19	6.16	1.12	Fe XII	249.388	0.69
						Fe XII	249.384	0.22
193.51	18200	1100.0	6.19	6.17	1.13	Fe XII	193.509	0.94
192.39	8090	559.0	6.19	6.17	1.02	Fe XII	192.394	0.96
195.12	27800	1450.0	6.19	6.17	1.23	Fe XII	195.119	0.97
200.02	1510	109.0	6.25	6.20	0.90	Fe XIII	200.021	0.94
246.21	170	185.0	6.25	6.20	0.80	Fe XIII	246.209	0.95
251.95	421	268.0	6.25	6.20	1.02	Fe XIII	251.952	0.96
204.94	180	59.2	6.25	6.20	1.18	Fe XIII	204.942	0.96
209.92	135	149.0	6.25	6.20	1.05	Fe XIII	209.916	0.95
202.04	5070	906.0	6.25	6.20	0.98	Fe XIII	202.044	0.96
264.79	858	239.0	6.29	6.20	0.99	Fe XIV	264.789	0.72
						Fe XI	264.772	0.24
274.20	835	240.0	6.29	6.22	1.05	Fe XIV	274.204	0.94
252.20	58	36.3	6.29	6.22	1.20	Fe XIV	252.200	0.94
211.32	370	418.0	6.29	6.22	1.06	Fe XIV	211.317	0.96
257.40	180	70.1	6.29	6.22	1.14	Fe XIV	257.394	0.96
270.52	398	112.0	6.29	6.22	0.99	Fe XIV	270.521	0.96
284.16	445	386.0	6.34	6.24	1.23	Fe XV	284.163	0.96

28−June−2019 − Fe XII

1: (2−36 186.85 Å+3−39,186.89 Å) I_{ob}=487
2: (1−30 192.39 Å) I_{ob}=559
3: (1−29 193.51 Å) I_{ob}=1100
4: (1−27 195.12 Å+2−33,195.18 Å) I_{ob}=1450
5: (3−34 196.64 Å) I_{ob}=128
6: (3−32 203.73 Å) (bl) 0.8xI_{ob}=120

28−June−2019 − Si X

1: (1−10 253.79 Å) I_{ob}=115
2: (2−10 258.37 Å) I_{ob}=546
3: (2−9 261.06 Å) I_{ob}=273
4: (1−8 271.99 Å) I_{ob}=226
5: (2−8 277.26 Å) I_{ob}=181

28−June−2019 − Fe XIII

1: (4−26 196.52 Å) I_{ob}=40.0
2: (2−24 200.02 Å) I_{ob}=109
3: (1−20 202.04 Å) I_{ob}=906
4: (3−25 203.83 Å+3−24,203.79 Å) I_{ob}=449
5: (3−20 209.92 Å) I_{ob}=149

28−June−2019 − Fe XIV

1: (1−11 211.32 Å $^2P_{1/2}-^2D_{3/2}$) I_{ob}=418
2: (1−10 252.20 Å $^2P_{1/2}-^2P_{3/2}$) I_{ob}=36.0
3: (1−9 257.39 Å $^2P_{1/2}-^2P_{1/2}$) (bl) I_{ob}=70.0
4: (2−10 264.79 Å $^2P_{3/2}-^2P_{3/2}$) (bl Fe XI) 0.7xI_{ob}=167
5: (2−9 270.52 Å $^2P_{3/2}-^2P_{1/2}$) I_{ob}=112
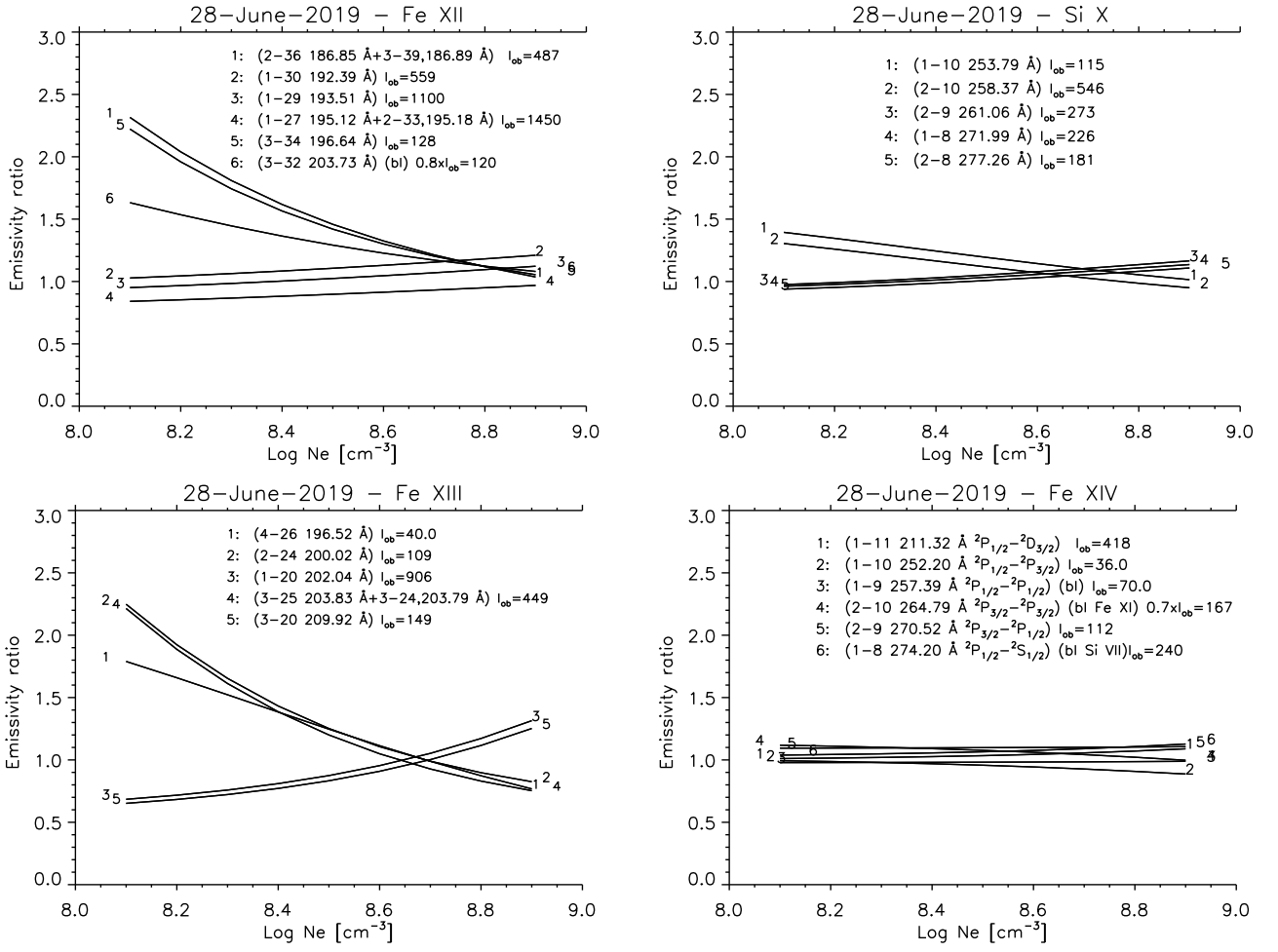6: (1−8 274.20 Å $^2P_{1/2}-^2S_{1/2}$) (bl Si VII)I_{ob}=240

Figure 15. Emissivity ratios of a selection of EIS lines for the off-limb quiet Sun observation of 2019-06-28.
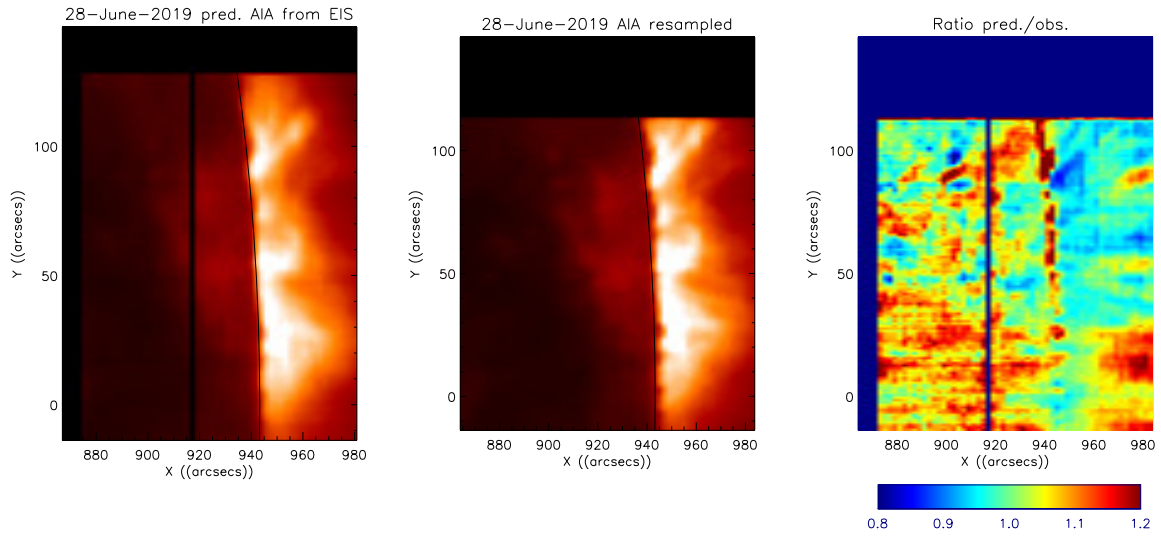
Figure 16. Results of the analysis to obtain the EIS SW radiometric calibration relative to AIA 193 Å.
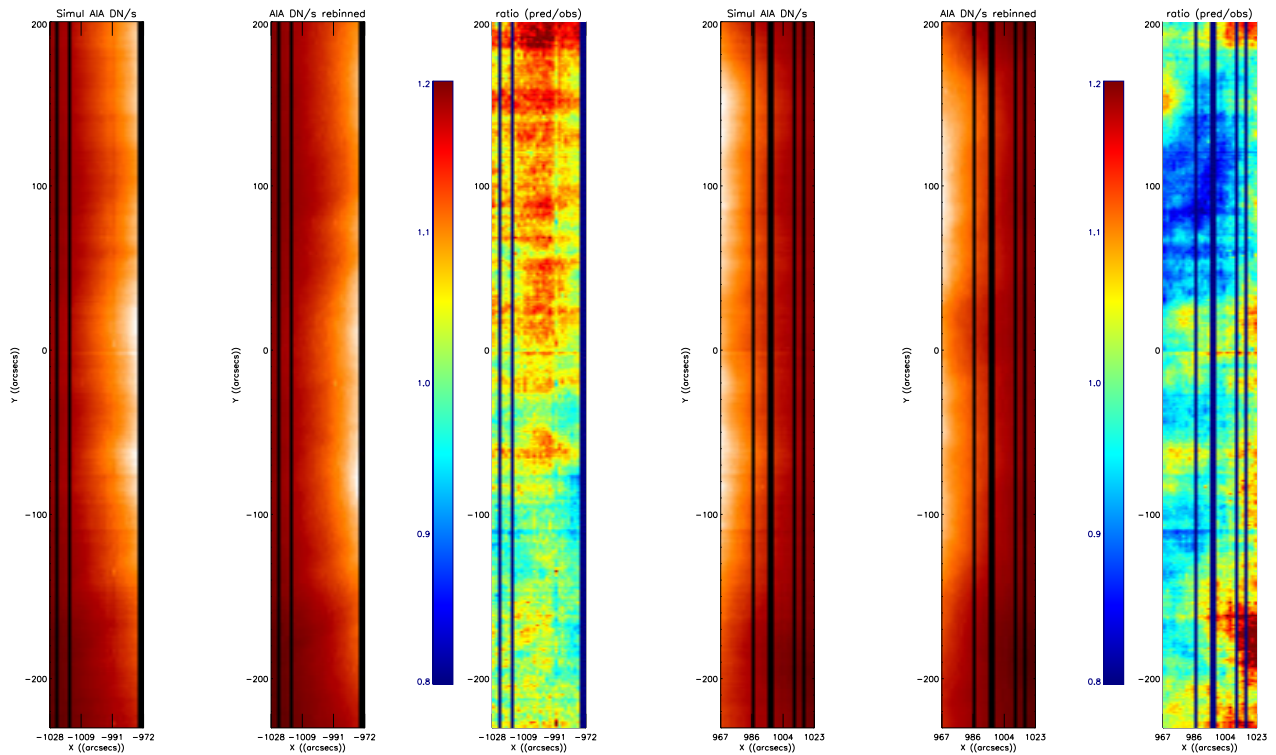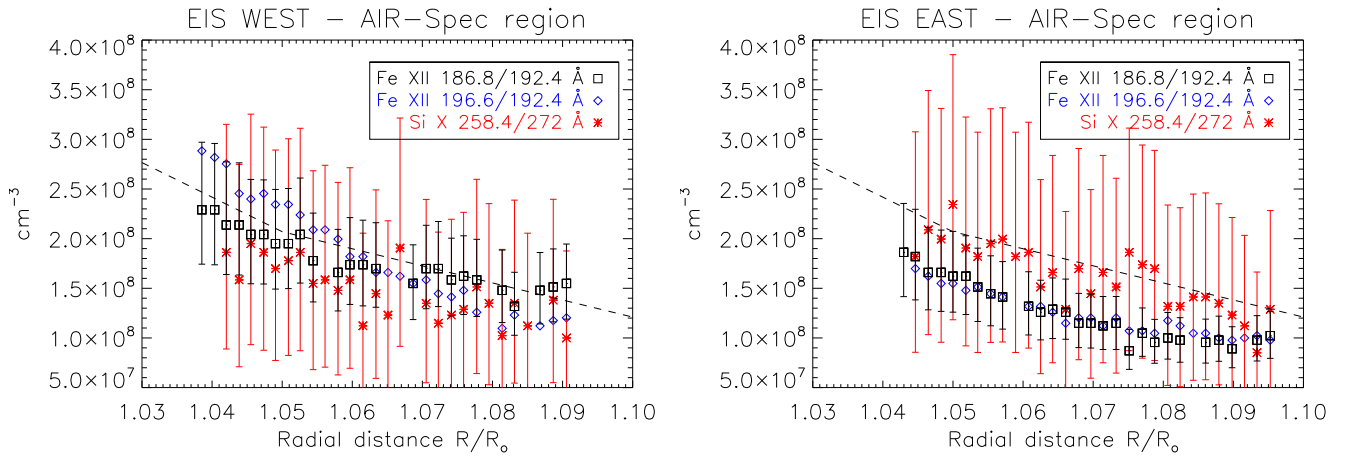

Figure 17. Results of the analysis to obtain the EIS off-limb pointing in the east and west, by comparing the predicted AIA signal with the observed one.

Figure 18. Electron densities obtained from a selection of EIS line ratios on the west and east regions. The dashed line indicates the expected radial density profile for the quiet Sun, from Del Zanna et al. (2018).